Pharmacological Research 208 (2024) 107353

Contents lists available at ScienceDirect

Pharmacological Research

journal homepage: www.elsevier.com/locate/yphrs

A novel combinatory treatment against a CDDP-resistant non-small cell lung cancer based on a Ruthenium(II)-cyclopentadienyl compound

Iris C. Salaroglio [a], Denitsa Stefanova [b], Ricardo G. Teixeira [c], Nuno F.B. Oliveira [d], Amer Ahmed [e,1], Fabio Fusi [f], Virginia Tzankova [b], Yordan Yordanov [b], Miguel Machuqueiro [d], Simona Saponara [e], Andreia Valente [c,*], Chiara Riganti [a,*]

[a] Department of Oncology and Molecular Biotechnology Center "Guido Tarone", University of Torino, piazza Nizza 44, 10126 Torino, Italy
[b] Medical University of Sofia, Faculty of Pharmacy, Department of Pharmacology, Pharmacotherapy and Toxicology, 2 Dunav Str., Sofia 1000, Bulgaria
[c] Centro de Química Estrutural, Institute of Molecular Sciences and Departamento de Química e Bioquímica, Faculdade de Ciências, Universidade de Lisboa, Campo Grande, Lisboa 1749-016, Portugal
[d] BioISI – Instituto de Biossistemas e Ciências Integrativas, Departamento de Química e Bioquímica, Faculdade de Ciências, Universidade de Lisboa, Lisboa 1749-016, Portugal
[e] University of Siena, Department of Life Sciences, via Aldo Moro, 2, Siena 53100, Italy
[f] University of Siena, Department of Biotechnologies, Chemistry and Pharmacy, via Aldo Moro 2, Siena 53100, Italy

ARTICLE INFO

Keywords:
Cisplatin resistance
ruthenium-cyclopentadienyl
non-small cell lung cancer
biocompatibility
cardiovascular toxicity

Chemical Compounds studied in this article:
Cisplatin (5702198)
Carboplatin (426756)

ABSTRACT

The therapeutic approach to many solid tumors, including non-small cell lung cancer (NSCLC), is mainly based on the use of platinum-containing anticancer agents and is often characterized by acquired or intrinsic resistance to the drug. Therefore, the search for safer and more effective drugs is still an open challenge.

Two organometallic ruthenium(II)-cyclopentadienyl compounds $[Ru(\eta^5\text{-}C_5H_4CHO)(Me_2bipy)(PPh_3)]^+$ (**RT150**) and $[Ru(\eta^5\text{-}C_5H_4CH_2OH)(Me_2bipy)(PPh_3)][CF_3SO_3]$ (**RT151**) were tested against a panel of cisplatin-resistant NSCLC cell lines and xenografts. They were more effective than cisplatin in inducing oxidative stress and DNA damage, affecting the cell cycle and causing apoptosis. Importantly, they were found to be inhibitors of drug efflux transporters. Due to this property, the compounds significantly increased the retention and cytotoxicity of cisplatin within NSCLC cells. Notably, they did not display high toxicity *in vitro* against non-transformed cells (red blood cells, fibroblasts, bronchial epithelial cells, cardiomyocytes, and endothelial cells). Both compounds induced vasorelaxation and reduced endothelial cell migration, suggesting potential anti-angiogenic properties. **RT151** confirmed its efficacy against NSCLC xenografts resistant to cisplatin. Either alone or combined with low doses of cisplatin, **RT151** showed a good biodistribution profile in the liver, kidney, spleen, lung, and tumor. Hematochemical analysis and post-mortem organ pathology confirmed the safety of the compound *in vivo*, also when combined with cisplatin.

To sum up, we have confirmed the effectiveness of a novel class of drugs against cisplatin-resistant NSCLC. Additionally, the compounds have a good biocompatibility and safety profile.

Abbreviations: NSCLC, non-small cell lung cancer; CDDP, cisplatin; MDR, multidrug resistance; ABC, ATP binding cassette; P-gp/ABCB1, P-glycoprotein; MRP-1/ABCC1, multidrug-resistant-associated protein-1; BCRP/ABCG2, breast cancer resistance protein; RuCp, ruthenium(II)-cyclopentadienyl derivatives; FBS, fetal bovine serum; MTT, 3–4,5-dimethylthiazol-2-yl-2,5-diphenyltetrazolium bromide; HAT, hypoxanthine-aminopterin-thymidine solution; BSA, bovine serum albumin; TEA^+, tetraethylammonium chloride; HDFa, human dermal adult fibroblasts; HSAEC, human small airway epithelial cells; ISIMA, ilastik segmentation/ImageJ measurement of area; CCD, Charged Coupled Device; ROS, Reactive oxygen species; CM-H2DCFDA, 5-and-6-chloromethyl-2′,7′-dichlorodihydro-fluorescein diacetate; RFUs, relative fluorescence units; 8OHdG, 8-hydroxy-2'-deoxyguanosine; Pi, phosphate; KHS, Krebs-Henseleit solution; NSG, NOD SCID-γ; ICP-MS, inductively coupled plasma mass spectrometry; SD, standard deviation.

* Corresponding authors.
E-mail addresses: amvalente@ciencias.ulisboa.pt (A. Valente), chiara.riganti@unito.it (C. Riganti).
[1] Current address: Department of Bioscience, Biotechnology and Environment, University of Bari, Via Edoardo Orabona, 70125 Bari, Italy.

https://doi.org/10.1016/j.phrs.2024.107353
Received 1 April 2024; Received in revised form 15 August 2024; Accepted 15 August 2024
Available online 17 August 2024

1. Introduction

Lung cancer (LC) is one of the most frequent types of cancer and the leading cause of cancer-related death globally, with an estimated 2.2 million new cases and 1.79 million deaths in 2020 [1]. LC is grouped into two main forms: small cell lung cancer and non-small cell lung cancer (NSCLC), with the latter accounting for 85 % of all cases [1]. Currently, the standard first-line chemotherapeutics used in NSCLC include three platinum-containing drugs approved worldwide: cisplatin (CDDP), carboplatin, and oxaliplatin [2]. Despite their efficacy, this approach is associated with side effects and, more importantly, with the development of drug resistance [3]. These two main setbacks have motivated researchers to actively search for alternatives based on non-platinum metallodrugs.

Over the last decades, ruthenium-based compounds emerged as part of a new era of chemotherapeutic candidates to treat cancer [4]. Many ruthenium-based compounds consistently show a broader spectrum of action, lower systemic toxicity, and are more selective to cancer cells [5, 6] than CDDP-inspired drugs, thus being proposed as promising therapeutic alternatives.

Ruthenium has three biologically accessible oxidation states (II, III, and IV) and their species can exert their activity *via* multiple targets, resulting in different mechanisms of action, and pharmacological responses [6]. Despite their promising anticancer properties, only two Ru (III) compounds (namely **NAMI-A**, designed by the group of Sava, Mestroni and Alessio [7] and **KP1019/NKP1339**, proposed by Keppler and coworkers [8]), along with one Ru(II) photosensitizer compound (**TLD1334**, developed by McFarland and collaborators [9]) have proceeded into clinical trials.

One of the major hurdles in cancer therapy is the development of mechanisms that limit the effectiveness of the chemotherapeutic agents. Some of these mechanisms, termed multidrug resistance (MDR), are characterized by the overexpression of efflux transporters (*e.g.*, ATP binding cassette – ABC – protein family) on the cancer cell membrane [10] P-glycoprotein (P-gp/ABCB1), multidrug resistance-associated protein-1 (MRP-1/ABCC1), and breast cancer resistance protein (BCRP/ABCG2) are among the ABC transporters most often associated with MDR and leading to patient poor prognosis. Particularly, P-gp and MRP1 transport several cytotoxic drugs including CDDP, limiting their intracellular accumulation, thus affecting therapeutic outcomes. Over the years, many researchers have developed novel P-gp modulators (mainly organic molecules) as prospective candidates to reverse MDR. However, despite these efforts, all generations of P-gp inhibitors tested so far failed due to their low specificity and high toxicity [11].

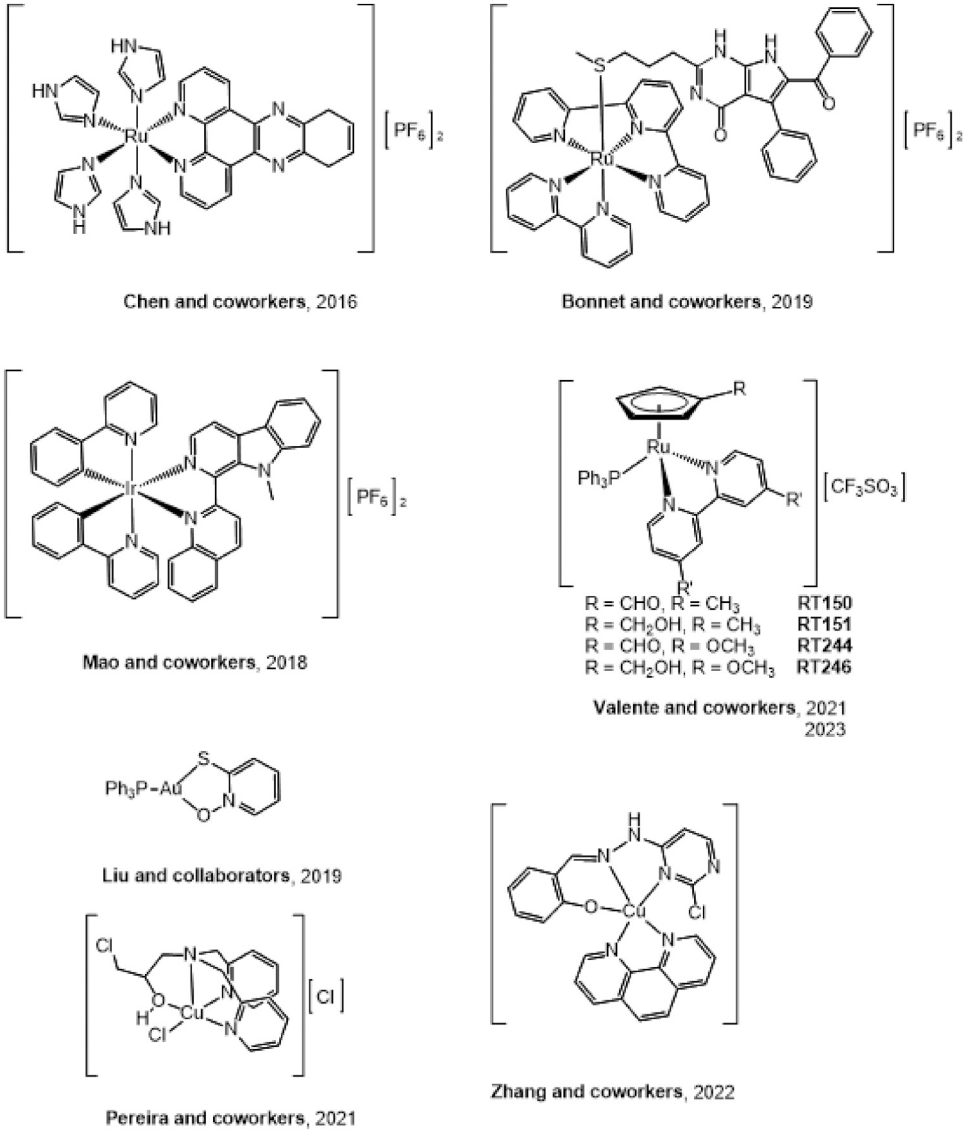

Scheme 1. Metal-based drugs with antitumoral activity towards non-small cell lung adenocarcinoma A549.

Therefore, searching for novel candidates capable of overcoming MDR with a good safety profile is crucial and still represents a key clinical challenge.

Non-platinum-based metallodrugs are emerging as important chemotherapeutic agents and promising alternatives to platinum-based drugs currently in clinical use as they have better safety profiles, and their cytotoxicity involves different mechanisms of action [12]. However, despite some promising *in vitro* results [13], only a few studies evaluating the efficacy of metal-based drugs on resistant LC xenografts were reported with encouraging and convincing results. For example, two ruthenium(II) complexes, namely $[Ru^{II}(Im)_4(dppz)][PF_6]_2$ (where Im = imidazole and dppz = 10,13-dihydrodipyrido[3,2-*a*:2′,3′-*c*]phenazine) [14], and the photosensitizer $[Ru^{II}(bipy)(tpy)(^{S}L)][PF_6]_2$ (where bipy = 2,2'-bipyridine, tpy = 2,2′:6′,2''-terpyridine and ^{S}L = 6-benzoyl-2-(3-(methylthio)propyl)-5-phenyl-1*H*-pyrrolo[2,3-*d*]pyrimidin-4(7*H*)-one) [15] (Scheme 1) were well tolerated and effective in reducing NSCLC grow in nude mice. Also the gold(I) complex $[Au^{I}(PPh_3)(PT)]$ [16] (where PT is pyrithione), and the iridium(III) complex $[Ir^{III}(ppy)_2(^{N,N}L)][PF_6]_2$ [17] (where ppy = 2-phenylpyridine and $^{N,N}L$ = 9-methyl-1-(quinolin-2-yl)-9*H*-pyrido[3,4-*b*]indole) showed similar results, the latter being more effective than CDDP. More recently, two copper(I)/(II) compounds (Scheme 1) of chemical formula $[Cu^{I}(^{O,N,N}L)(phen)]$ (with $^{O,N,N}L$ being a Schiff base like ligand and phen = 1,10-phenanthroline) [18] and $[Cu^{II}(^{N,N,N,O}L)Cl][Cl]$ [19] (where $^{N,N,N,O}LH$ is 1-[bis(pyridine-2-ylmethyl)amino]-3-chloropropan-2-ol) showed promising anti-tumor activity against A549 xenografts; noticeably, the Cu(II) complex in association with CDDP demonstrated also the added value of the presence of a second metal in a combinatorial therapy.

In this scenario, organometallic ruthenium(II)-cyclopentadienyl derivatives ('RuCp') are emerging as promising cytotoxic agents against several aggressive cancer cell lines and, particularly, as chemosensitizers in NSCLC cell lines [20,21]. By impairing the activity of P-gp and MRP1 transporters [20–22], they overcame CDDP resistance, paving a new avenue to treat resistant NSCLC through a possible synergism with CDDP. However, a consistent correlation between *in vitro* and *in vivo* results is still lacking. To this aim, the most promising ruthenium (II)-cyclopentadienyl derivatives **RT150** and **RT151**, showing selectivity and exceptional cytotoxicity towards several CDDP-resistant cell lines, along with low activity against CDDP-sensitive cells, were investigated in depth to define their mechanism of action, alone and in association with CDDP. Their biocompatibility and efficacy were explored *in vivo*, with the final goal of developing a novel, valuable combinatorial treatment, effective against CDDP-resistant NSCLC.

2. Materials and methods

2.1. Chemicals

Fetal bovine serum (FBS), RPMI-1640 and DMEM cell culture media, L-glutamine, trypsin/EDTA solution and 3-(4,5-dimethylthiazol-2-yl)-2,5-diphenyltetrazolium bromide (MTT), hypoxanthine-aminopterin-thymidine solution (HAT), collagenase (type XI), trypsin inhibitor, bovine serum albumin (BSA), tetraethylammonium chloride (TEA^+), phenylephrine, acetylcholine, and nifedipine were provided by Sigma Aldrich (Schnelldorf, Germany) and sodium nitroprusside was from Riedel-De Haën AG (Seelze-Hannover, Germany). All other substances were of analytical grade and used without further purification.

2.2. Preparation of the compounds under study – RT150 and RT151

Both ruthenium-cyclopentadienyl compounds (general formula $[Ru(\eta^5\text{-}C_5H_4R)(Me_2bipy)(PPh_3)][CF_3SO_3]$, where R = CHO (**RT150**) or CH_2OH (**RT151**), PPh_3 is triphenylphosphane and Me_2bipy is 4,4'-dimethyl-2,2'-bipyridine) were prepared under nitrogen atmosphere by using standard *Schlenk* techniques as previously described [20]. Stock solutions of **RT150** and **RT151** used in *in vitro* studies were prepared in DMSO and further dilutions in cell culture medium were done to achieve the final concentrations. For *in vivo* studies, samples were prepared by using 40 % w/v Captisol® in ultrapure water (MilliQ, 18.2 MΩ × cm) as the solubilizing agent to achieve the desired doses. Solutions of **RT151** (0.2–0.8 mg/mL) in water were prepared by first crushing **RT151** and Captisol® with a mortar and pestle until a homogeneous mixture was obtained. The mixture was then transferred to a plastic container and slowly diluted with ultrapure water using sonication between additions. The final solutions were placed in a mechanical shaker with continuous stirring overnight, filtered with 20 μm filters, and stored at −20 °C until use. The stability of **RT150** and **RT151** in DMSO (100 %) and DMEM (with 2 % DMSO as co-solvent to solubilize the compound in aqueous media) was previously reported in ref. [20]. In addition, the chemical stability of **RT151** encapsulated in Captisol® was assessed by measuring the absorption spectra using UV-Vis spectrophotometry, at room temperature, for 4 weeks.

2.3. Cell lines

Human NSCLC A549, Calu-3, NCI-H2228, NCI-H1650, and NCI-H1975 were purchased from ATCC (Manassas, VI), and maintained in RPMI-1640 medium containing 10 % v/v FBS and 1 % penicillin-streptomycin. NCI-H1650/CDDP and NCI-H1975/CDDP sublines were generated by adding CDDP in the culture medium, at increasing concentrations (1 pM, 10 pM, 100 pM, 1 nM, 10 nM, 100 nM) every 2 weeks. Cells were then maintained in RPMI-1640 medium containing 100 nM CDDP. Primary human dermal adult fibroblasts (HDFa, ATCC-PCS-201–012™) were cultured in the Fibroblast Basal Media supplemented with Fibroblast Growth Kit (ATCC). Primary human small airway epithelial cells (HSAEC, ATCC-PCS-301–010™) were maintained in Airway Epithelial Cell Basal Media supplemented with Bronchial Epithelial Cell Growth Kit (ATCC). Rat myoblast cell line H9c2 (ECACC, Salisbury, UK) was cultured in DMEM high glucose medium, supplemented with 10 % v/v heat-inactivated FBS, 2 mM L-glutamine, and 1 mM sodium pyruvate. Human macrovascular endothelial cell line EA.hy926 (ATCC-CRL-2922™) was cultured in DMEM supplemented with HAT, as previously described [23]. Cell culture was propagated in 75 cm^2 flasks and kept in an incubator, maintaining 37 °C, 5 % CO_2 and high humidity. All cells were sub-cultured by trypsinization when they reached sub-confluence.

2.4. Viability assays

A549, Calu-3, NCI-H2228, NCI-H1650, NCI-H1650/CDDP, NCI-1975, NCI-1975/CDDP, HDFa, HSAEC, H9c2 (10^4 per well), EA.hy926 (2×10^4 per well) cells were treated with CDDP, **RT150** or **RT151**, in the range of concentration from 1 nM to 10 μM for 24, 48 or 72 h, renewing the solution every 24 h. At each time point, the MTT assay was performed as previously described [24]. The reduction of cell viability by more than 20 % was considered a cytotoxic effect (ISO 10993 2009, [25]). The absorbance was measured in a Synergy 2 microplate reader (BioTek Instruments Inc., Winooski, VT) at 540 nm [26]. The Combination Index (CI) was calculated according to the Chou-Talalay method [27], using the CalcuSyn software (www.biosoft.com/w/calcusyn.htm).

2.5. Apoptosis evaluation

Since apoptosis in cell culture is often accompanied by morphological changes such as loss of adhesion and rounded shape of cells [28–30] the amount of H9c2 rounded cells after treatment with **RT150** and **RT151** was measured by combined ilastik segmentation/ImageJ measurement of area (ISIMA) approach, described by Yordanov and co-workers [31]. Images were taken with an 8-megapixel CCD (Charged Coupled Device) digital camera (Optikam Pro 8LT-4083.18LT), mounted on an inverted Optika XDS-2 microscope, illuminated by a

X-LED8TM system. The following settings were applied: phase contrast mode and 100x magnification. The image segmentation into rounded morphology cells (foreground pixels) and adherent cells or plate surface (background pixels) was done on the ilastik software, version 1.3.3b2 (BSD type license, open source, available for free download at www.ilastik.org). The resulting black and white images were used for foreground (rounded morphology cells) area measurement in the ImageJ software, version 2.0.0-rc-43/1.50e (BSD type license, open source, www.imagej.net) [32]. As a result, area percentage values were estimated.

For A549, Calu-3 and NCI-H2228 cells, the Annexin V/Propidium Iodide staining was used. Cells were detached with the Cell Dissociation Solution (Sigma-Merck) and stained with the Annexin V/Propidium Iodide kit (Sigma-Merck), as per manufacturer instruction. Fluorescence was acquired using a Guava® easyCyte flow cytometer (InCyte software, Millipore, Burlington, MA). The percentage of Annexin V^+/Propidium $Iodide^+$ cancer cells was considered an index of necro-apoptotic death.

2.6. Reactive oxygen species (ROS) measurement

A549, Calu-3, and NCI-H2228 cells (1×10^6) were washed with PBS and detached by gentle scraping. A 50 µL aliquot was sonicated and used to measure cell proteins. The remaining cells were incubated for 30 min at 37 °C with 5 µM ROS-sensitive fluorescent probe 5-(and-6)-chloromethyl-2′,7′-dichlorodihydro-fluorescein diacetate (CM-H_2DCFDA) (ThermoFisher Invitrogen, Milan, Italy). The fluorescence was read using a Synergy 2 microplate reader, with λ excitation 485 nm and λ emission 528 nm. The relative fluorescence units (RFUs) were converted into nanomoles ROS/mg proteins, according to a titration curve performed with serial dilutions of H_2O_2.

2.7. DNA oxidative damage

The amount of 8-hydroxy-2'-deoxyguanosine (8OHdG), considered an index of oxidized and damaged DNA [33], was measured in A549, Calu-3, and NCI-H2228 cells by the 8OHdG ELISA Kit (Abcam, Cambridge, UK), as per manufacturer instructions. Results were expressed as nmoles of 8OHdG/mg cell proteins.

2.8. Cell cycle evaluation

For the cell cycle analysis, 1×10^5 A549, Calu-3, and NCI-H2228 cells were fixed in 70 % v/v ethanol for 15 min, then centrifuged at 13,000×*g* for 5 min at 4 °C, rinsed with citrate buffer (50 mM Na_2HPO_4, 25 mM sodium citrate, 1 % v/v Triton X-100) containing 1 µg/mL propidium iodide and 1 µg/mL RNAse, and analyzed after 15 min incubation in the dark. For each flow cytometry analysis, 20,000 events were collected using the Guava®easyCyte flow cytometer. Cell cycle distribution was analyzed using the InCyte software.

2.9. ABCB1 and ABCC1 activity

The catalytic activity of immunopurified ABCB1 and ABCC1, measured as the rate of ATP hydrolysis, was assessed spectrophotometrically at 620 nm with a Synergy 2 microplate reader, as previously described [21]. The results were expressed as nmoles hydrolyzed phosphate (P_i)/min/mg protein.

2.10. Intracellular carboplatin retention

A549, Calu-3, and NCI-H2228 cells (1×10^6) were incubated for 3 h with 1 µCi [^{14}C]-carboplatin (20 Ci/mmol; Amersham Bioscience, Piscataway, NJ), washed twice in PBS, detached with trypsin, centrifuged at 1300×*g* for 2 min and sonicated. The amount of [^{14}C]-carboplatin was detected by liquid scintillation and radioactivity converted into nmoles/mg cell proteins [34].

2.11. RT-PCR

Total RNA was extracted and reverse-transcribed using iScriptTM cDNA Synthesis Kit (Bio-Rad Laboratories, Hercules, CA). The qRT-PCR was performed with the IQ SYBR Green Supermix (Bio-Rad Laboratories). The primers used were: *ABCB1/P-gp*: forward: 5′-GAGGAAGACATGACCAGGTATGC-3', reverse: 5′-CCCACCCACCAAAATGAAACC-3'; *ABCC1/MRP1*: forward: 5′-TCTGGTCAGCCCAACTCTCT-3', reverse: 5′-CCTGTGATCCACCAGAAGGT-3'; *B2M*: forward: 5′-AGCAAGGACTGGTCTTTCTATCTC-3', reverse: 5′-ATCTCTCCATCCCACTTAAGTATCTT-3'. The relative quantification of the genes of interest was performed by comparing each PCR product with the housekeeping *B2M* gene, using the Bio-Rad Software Gene Expression Quantitation (Bio-Rad Laboratories).

2.12. Immunoblotting

Cells were lysed in MLB buffer (125 mM Tris-HCl, 750 mM NaCl, 1 % v/v NP40, 10 % v/v glycerol, 50 mM $MgCl_2$, 5 mM EDTA, 25 mM NaF, 1 mM $NaVO_4$, 10 mg/mL leupeptin, 10 mg/mL pepstatin, 10 mg/mL aprotinin, 1 mM phenylmethylsulphonyl fluoride, pH 7.5), sonicated and centrifuged at 13,000×*g* for 10 min at 4 °C. 50 µg of proteins, prior to the immunoprecipitation steps, were subjected to immunoblotting and probed with the following antibodies: anti-P-gp (clone C219, Novus Biologicals, Littleton, CO, dilution 1/250), anti-MRP1 (Santa Cruz Biotechnology Inc., Santa Cruz, CA, Cat: sc-18835 dilution 1/1000), anti-GAPDH (Santa Cruz Biotechnology Inc., Cat: sc-47724, dilution 1/1000). In immunoprecipitation assays, 100 µg of whole cell lysates were immunoprecipitated with an anti-α-ubiquitin (R&D Systems, Minneapolis, MI, IgG2B clone 83406, dilution 1/50), with the PureProteome Protein A/G Mix Magnetic Beads (LSKMAGAG10, Millipore) for 3 h at 4 °C, then immunoblotted for P-gp or MRP1. The proteins were detected by enhanced chemiluminescence (Bio-Rad Laboratories).

2.13. Flow cytometry

1×10^6 NCI-H2228 cells, washed in PBS containing 0.5 % bovine serum albumin (BSA) and 2 mM EDTA, were centrifuged at 300×*g* for 10 min, incubated 20 min at room temperature in the dark with 250 µl of Inside Fix reagent (Inside Stain Kit, Miltenyi Biotec., Bergisch Gladbach, Germany), centrifuged at 300×*g* for 5 min, washed with 1 mL of Inside Perm (Inside Stain Kit), centrifuged at 300 × g for 5 min, and incubated 30 min at room temperature with the following antibodies (dilution 1/50): anti-CD243/ABCB1 antibody (Miltenyi, clone REA495, PE-Vio® 770-conjugated); anti-MRP1/ABCC1 antibody (Miltenyi, clone REA481, PE-conjugated). Cells were washed with 1 mL of Inside Perm reagent, centrifuged at 300×g for 5 min and read using a Guava easyCyte Flow Cytometer, equipped with the Guava Incyte software.

2.14. Hemolysis assay

Healthy volunteer blood specimens were obtained from a certified clinical laboratory. The experimental procedures were conducted according to the rules of the Institutional Ethics Committee (KENIMUS) at the Medical University - Sofia, Bulgaria.

Erythrocytes were isolated by sequential centrifugation and resuspended in phosphate buffer at pH 7.4 [35]. The isolated red blood cells were pipetted in 96-well plates and co-incubated with compounds **RT150** and **RT151** (1–500 µM) in phosphate buffer at pH 7.4. Negative control wells containing vehicle and positive control wells containing a final concentration of 2 % v/v TritonX-100 were included. After 1 h, each plate was centrifuged, and supernatant aliquots were transferred to an empty plate. The amount of hemoglobin released in the supernatant was spectrophotometrically measured at 405 nm. The percentage of hemolysis was calculated as the fraction of lysed erythrocytes, according to the following equation:

$$\text{Hemolysis}(\%) = \frac{\text{Abs(sample)} - \text{Abs(negative control)}}{\text{Abs(TritonX} - 100) - \text{Abs(negative control)}} \times 100$$

2.15. EA.hy926 cells wound healing scratch assay

EA.hy926 cells (8×10^5) were seeded on the bottom of a 24-well plate and grown until confluence. A scratch was made by using a 200 μL sterile loading tip to create a wound across the cell monolayer. Thereafter, a basic medium containing 1 % FBS, 1 % cytosine arabinoside (to control cell proliferation), and **RT150** or **RT151** (1 μM and 5 μM) was added before incubation at 37 °C for 24 h. EA.hy926 cells were examined by a phase-contrast light microscope and images were captured with a digital camera at 0 h, 8 h, and 24 h at 5X magnification. Wells without treatments were used as control. Migration, evaluated as a hallmark of angiogenesis, was expressed as the percentage of scratch closure after 8 h and 24 h compared with the initial area at time 0. An optimized automated method to rapidly quantify the migration of adherent cells by ImageJ was used [36].

2.16. Ex-vivo and in vivo experiments

The experiments comply with the European Union Guidelines for the Care and the Use of Laboratory Animals (Directive 2010/63/EU) for experimental design and analysis in pharmacology care. The experimental studies were approved by the Animal Care and Ethics Committees of the University of Siena (experimental set: cardiovascular safety) and University of Turin (experimental set: tumor growth evaluation), and by the Italian Department of Health (approvals: #7DF19.N.SJQ for University of Siena; #54/2020 for University of Turin).

For cardiovascular safety experiments, male Wistar rats (250–350 g) were purchased from Charles River Italia (Calco, Italy) and maintained in an animal house facility at 25 ± 1 °C and 12:12 h dark-light cycle with access to standard chow diet and water *ad libitum*. Animals were anesthetized with isoflurane (4 %) and O_2 gas mixture using Fluovac (Harvard Apparatus, Holliston, Massachusetts, USA), decapitated, and exsanguinated. The thoracic aorta and tail main artery were immediately isolated and placed in a modified Krebs-Henseleit solution (KHS) or an external solution and prepared as detailed below.

For the tumor growth evaluation, in a preliminary experimental setting, female NOD SCID-γ (NSG; 20 ± 1.6 g/each) mice, housed (4 per cage) under 12 h light/dark cycle, with food and drinking provided *ad libitum*, were treated for 6 weeks (once/week) as it follows (4 mice/group): vehicle group, treated with 0.1 mL Captisol® intravenously (i.v.); **RT151** low dose group, treated with 3 mg/kg **RT151** i.v.; **RT151** medium dose group, treated with 6 mg/kg **RT151** i.v.; **RT151** high dose group, treated with 10 mg/kg **RT151** i.v., to select the maximum tolerated doses. In a second experimental setting, 1×10^6 A549 cells, mixed with 100 μL Matrigel (Sigma Aldrich), were injected subcutaneously (s.c.) in NSG mice. Tumor growth was measured daily by caliper, according to the equation $(LxW^2)/2$, where L=tumor length and W=tumor width. When tumors reached the volume of 50 mm^3, animals (5 mice/group) were randomized and treated for 6 weeks (once/week) as follows: vehicle group, treated with 0.1 mL Captisol® i.v.; CDDP group, treated with 5 mg/kg CDDP i.v.; **RT151** low dose group, treated with 3 mg/kg **RT151** i.v.; **RT151** medium dose group, treated with 6 mg/kg **RT151** i.v.; CDDP+**RT151** low dose group; CDDP+**RT151** medium dose group. Tumor volumes were monitored by caliper and animals were euthanized at day 42 (i.e. 7 days after the last treatment) with zolazepam (0.2 mL/kg) and xylazine (16 mg/kg). Animal weights were monitored throughout the study. Tumors were excised, sectioned, fixed in 4 % v/v paraformaldehyde, and stained with hematoxylin/eosin (Sigma Aldrich) or immunostained for Ki67 (Millipore), cleaved (Asp175)caspase-3, i.e. the active caspase 3 form (Cell Signaling Technology, Danvers, MA), followed by a peroxidase-conjugated secondary antibody (Dako, Santa Clara, CA). Nuclei were counterstained with hematoxylin (Sigma Aldrich). Sections were examined by a Leica DC100 microscope (Leica, Weitzlar, Germany), by analysing a minimum of 5 fields/tumor.

2.17. Biodistribution of RT151 in the mouse main organs

Immediately after the mice sacrifice, tumors, kidneys, lungs, liver, and spleen were collected and weighed. Organs were then washed twice in sterile PBS, homogenated using a Tissue Lyser II homogenizer (Qiagen, Hilden, Germany), and immediately snap-frozen for subsequent quantification of ruthenium and platinum by inductively coupled plasma mass spectrometry (ICP-MS). All samples were lyophilized, weighted, digested with freshly prepared *aqua regia* (1:3 HNO_3:HCl) and H_2O_2 (30 % vol), and then diluted in ultrapure water (MilliQ, 18.2 MΩxcm) to obtain up to 6 % (v/v) acid concentration. Platinum and ruthenium content in the different organs and tumors was measured by an ICP-MS Thermo X Series Quadrupole ICP-MS (Thermo Scientific) at Laboratório Central de Análises from Universidade de Aveiro, Portugal.

2.18. Hematochemical and post-mortem organ analyses

Following sacrifice, mouse organs (lung, liver, kidney, and spleen) were collected, fixed in 4 % v/v paraformaldehyde, and stained with hematoxylin/eosin to evaluate the gross pathology, analyzing a minimum of 5 fields for each organ. Immediately after the euthanasia, 200 μL blood was collected to measure the following parameters: red blood cells, white blood cells, hemoglobin and platelets as indexes of bone marrow function; lactate dehydrogenase, aspartate aminotransferase, alanine aminotransferase and alkaline phosphatase, as indexes of liver function; creatinine, as index of kidney function; creatine phosphokinase, as index of muscle/heart damage; cardiac troponin, as index of cardiac damage, using commercially available kits from Beckman Coulter Inc. (Miami, FL).

2.19. Rat tail main artery cell isolation procedure for patch-clamp experiments

Smooth muscle cells were freshly isolated from the rat tail main artery, at 37 °C, by 1.35 mg/mL collagenase (type XI) treatment in the presence of 1 mg/mL BSA and 1 mg/mL trypsin inhibitor, in 2 mL of 0.1 mM Ca^{2+} external solution (130 mM NaCl, 5.6 mM KCl, 10 mM HEPES, 20 mM glucose, 1.2 mM $MgCl_2$, and 5 mM sodium pyruvate; pH 7.4) containing 20 mM taurine, under a gentle stream of a 95 % O_2-5 % CO_2 gas mixture as previously described [37]. Cells stored in 0.05 mM Ca^{2+} external solution containing 20 mM taurine and 0.5 mg/mL BSA at 4 °C under normal air were used for experiments within two days after isolation [38].

2.20. Ba^{2+} current through $Ca_V1.2$ channel ($I_{Ba1.2}$) recordings

The conventional whole-cell configuration of the patch-clamp technique was employed to record $I_{Ba1.2}$ from freshly isolated vascular smooth muscle cells. Borosilicate recording electrodes (WPI, Berlin, Germany) had a pipette resistance of 2–4 MΩ when filled with an internal solution containing 100 mM CsCl, 10 mM HEPES, 11 mM EGTA, 1 mM $CaCl_2$ (pCa 8.4), 2 mM $MgCl_2 \cdot 6\,H_2O$, 5 mM sodium pyruvate, 5 mM succinic acid, 5 mM oxaloacetic acid, 3 mM Na_2-ATP, and 5 mM phosphocreatine; pH was adjusted to 7.4 with CsOH. An Axopatch 200B patch-clamp amplifier (Molecular Devices Corporation, Sunnyvale, CA, USA) in conjunction with an ADC/DAC interface (DigiData 1200 A/B series, Molecular Devices Corporation) was used to: generate and apply voltage pulses and record the corresponding membrane currents; adjust to zero the junction potential between the pipette and bath solution; compensate whole-cell capacitance and series resistance (between 70 % and 75 %). Current signals were low-pass filtered at 1 kHz and digitized

at 3 kHz before being stored on the computer hard disk. Cells were continuously superfused, at room temperature (20–22 °C), with an external solution containing 0.1 mM Ca^{2+} and 30 mM TEA^{+} using a peristaltic pump (LKB 2132, Bromma, Sweden), at a flow rate of 400 μL/min.

$I_{Ba1.2}$ was recorded in an external solution containing 30 mM TEA^{+} and 5 mM Ba^{2+}. The current was elicited with 250-ms clamp pulses (0.067 Hz) to 10 mV from a holding potential (V_h) of −50 mV. Data were collected once the current amplitude had been stabilized (usually 7–10 min after the whole-cell configuration had been obtained). Then the various experimental protocols were performed as detailed below. Under these conditions, $I_{Ba1.2}$ did not run down during the following 30–40 min [39]. K^{+} currents were blocked with 30 mM TEA^{+} in the external solution and Cs^{+} in the internal solution. Current values were corrected offline for leakage and residual outward currents using 10 μM nifedipine, which completely blocked $I_{Ba1.2}$.

2.21. Rat aorta ring preparation

The thoracic rat aorta was gently cleaned of adipose and connective tissues and cut into 3–4-mm wide rings. These were mounted in organ baths at 37 °C filled with KHS solution (118 mM NaCl, 4.75 mM KCl, 1.19 mM KH_2PO_4, 1.19 mM $MgSO_4$, 25 mM $NaHCO_3$, 11.5 mM glucose, 2.5 mM $CaCl_2$, gassed with a 95 % O_2-5 % CO_2 gas mixture to create a pH of 7.4), between two parallel, L-shaped, stainless steel hooks, one fixed in place and the other connected to an isometric transducer (BLPR, WPI, Berlin, Germany; [40]). Rings were allowed to equilibrate for 60 min in KHS under a passive tension of 1 g. During this equilibration period, the solution was changed every 15 min. Isometric tension was recorded using a digital PowerLab data acquisition system (PowerLab 8/30; ADInstruments). Ring viability was assessed by recording the response to 0.3 μM phenylephrine and 60 mM KCl. The endothelium was removed by gently rubbing the lumen of the ring with a forceps tip. This procedure was validated by adding 10 μM acetylcholine at the plateau of phenylephrine-induced contraction: a relaxation <15 % denoted the absence of functional endothelium [41].

2.22. Effect of RT150 and RT151 on rat aorta rings stimulated by either phenylephrine or high KCl concentrations

Rat aorta rings were pre-contracted pharmaco-mechanically by 0.3 μM phenylephrine or electro-mechanically by 60 mM KCl [42]. Once the contraction reached a plateau, **RT150** or **RT151** compound was added cumulatively into the organ bath to assess its vasorelaxant activity. At the end of the concentration-response curve, 100 μM sodium nitroprusside alone (phenylephrine-induced contraction) or 1 μM nifedipine followed by sodium nitroprusside (K^{+}-induced contraction) were added to test the functional integrity of smooth muscle. Vasodilation was calculated as a percentage of the contraction induced by either phenylephrine or KCl.

2.23. Homology modeling

To date, no human MRP1 crystal structure has been produced and the highest homology structure available (~91 % sequence similarity) is from *Bos taurus* (PDBid: 5UJ9). Hence, AlphaFold-2 [43] and homology modeling were used as starting points for the human MRP1 structure. In a standard homology modeling protocol with the MODELLER package [44], the full structure of *Bos taurus* was used as a template and aligned with the full human MRP1 sequence. However, the solutions obtained with this approach showed unrealistic relative domain positioning. To overcome this problem, the protein sequence was split into 4 parts (TMD1, TMD2, NBD1, and NBD2) and the homology modeling protocol was performed for each segment of the *Bos taurus* structure. Fifty structures for each of the protein's parts were obtained, the best model was selected through the DOPE score and the Ramachandran plot [45] was used for confirmation. The final 4 structure segments were assembled using PYMOL [46], aligning the human protein domains to the bovine template structure.

2.24. Molecular docking

Similarly to our previous docking protocol for P-gp [21], the Autodock Vina 1.2 software [47] was used to perform the docking of the ruthenium base complexes **RT150** and **RT151** in the MRP1 structure. All structures of MRP1 and complexes, as well as the docking box, were generated using AutoDockTools 4 [48], with Kollman charges [49] on the protein and Gasteiger charges [50] on the ruthenium-based complexes. As ADT4 is unable to assign the correct charge for ruthenium and phosphorus, we implemented the Mulliken charges (+0.38 and +0.6, respectively), obtained from a QM optimization of TM34 [51]. Three different structures were used in the docking protocol: *Bos taurus*, human AlphaFold 2 model and human homology modeling. The human structures were aligned to the bovine one to allow the use of the same docking box. The docking box sampled in this work used a grid spacing of 1.0 Å and a size of 50x50x50 nodes. A total of 30 solutions were requested in each software run.

2.25. Statistical analysis

All statistical analyses of experimental data have been done on GraphPad Prism 6 Software (La Jolla, CA). The data from at least 3 independent experiments are presented as the arithmetic mean ± standard deviation (SD). Significance testing was performed using Student's t-test for paired samples (two-tailed), multiple t-tests with Holm-Sidak correction for comparing series of samples at identical concentrations, or one-way ANOVA followed by Dunnet's post-test. Values of $^{*}p < 0.05$, $^{**}p < 0.01$, and $^{***}p < 0.001$ were considered significant.

3. Results

3.1. RT150 and RT151 induce oxidative stress and apoptosis in non-small cell cancer cells bypassing the resistance to cisplatin

RT150 and **RT151** increased intracellular ROS more than CDDP in CDDP-resistant NSCLC A549, Calu-3, and NCI-H2228 cell lines, when used at 0.1 μM (i.e., 34–116 times lower than their IC_{50} values in the corresponding cell lines [21]; Fig. 1A). Oxidative stress was further increased when the compounds were combined with CDDP (Fig. 1A). Consistently, both ruthenium derivatives induced oxidative stress on DNA (Fig. 1B) that resulted in increased percentage of cells arrested in S-phase, indicative of DNA damage, reduced amount of cells in mitotic progression (G2/M phase), increased percentage of apoptotic sub-G1 cells (Fig. 1C), and necro-apoptosis (Fig. 1C-D), while CDDP was devoid of effects on all these parameters. Using **RT150** and **RT151** in combination with CDDP also resulted in increased oxidative DNA damage, impairment of the cell cycle, and cell death (Fig. 1B-D). **RT151** was slightly more effective than **RT150** in all the experimental settings.

In line with previous findings indicating an inhibitory effect of ruthenium-derivatives on ABC transporters [21], a decrease in P-gp and MRP1 activity in cells treated with **RT150** and **RT151** was found, even in the presence of CDDP (Fig. 2A-B). Notably, the intracellular retention of the drug was significantly increased (Fig. 2C).

It has been recently demonstrated that **RT150** and **RT151** bind to P-gp to exert their inhibitory effects [21]. There are no X-ray structures for the human MRP1 protein. Hence, the AlphaFold model was compared [43] with the highest homology X-ray structure available, which is from *Bos taurus*. Visual close inspection showed that the AlphaFold model has a significantly more closed internal cavity (Fig. 3A-B), which could have a large impact on the molecular docking protocol. Using homology modeling, another model structure that was more open, similar to the one from *Bos taurus*, was generated (Fig. 3A-B). All three structures were

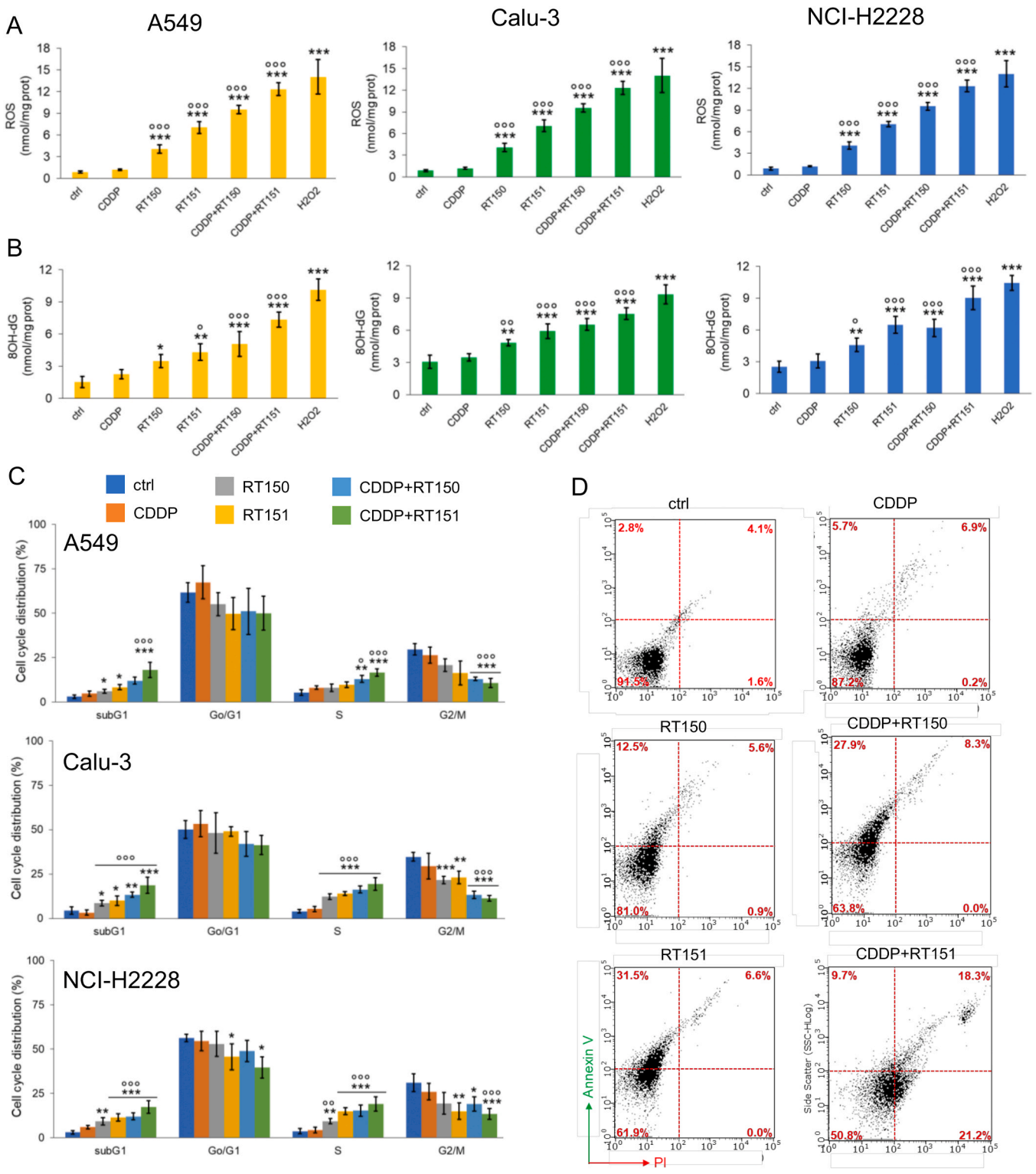

Fig. 1. RT150 and RT151 induced oxidative DNA damage and cell cycle arrest in cisplatin-resistant non-small cell lung cancer cell lines. Human non-small cell lung cancer A549, Calu-3, and NCI-H2228 cells were incubated for 6 h (**A-B**) or 24 h (**C-D**) with fresh medium (ctrl), 50 μM cisplatin (CDDP), 0.1 μM **RT150** or **RT151**, individually or in combination. When indicated, 1 μM H_2O_2 was used as positive control and was added 10 min before the assays. **A.** ROS fluorimetric measurement, in technical duplicates. Data are expressed as mean ± SD (n = 3 independent experiments). ***p < 0.001 vs ctrl; °°°p < 0.001 vs CDDP alone. **B.** Amount of 8-hydroxy-2'-deoxyguanosine (8OHdG), as an index of DNA damage, measured by ELISA in technical duplicates. Data are expressed as mean ± SD (n = 3 independent experiments). *p < 0.05, **p < 0.01, ***p < 0.001 vs ctrl; °p < 0.05, °°p < 0.01, °°°p < 0.001 vs CDDP alone. **C.** Cell cycle analysis, measured by flow cytometry in technical duplicates. Data are expressed as mean ± SD (n = 3 independent experiments). *p < 0.05, **p < 0.01, ***p < 0.001 vs ctrl; °p < 0.05, °°p < 0.01, °°°p < 0.001 vs CDDP alone. **D.** Representative dot-plots of Annexin V^+/PI^+ cells, index of necro-apoptotic cells. Images are representative of 3 experiments with comparable results.

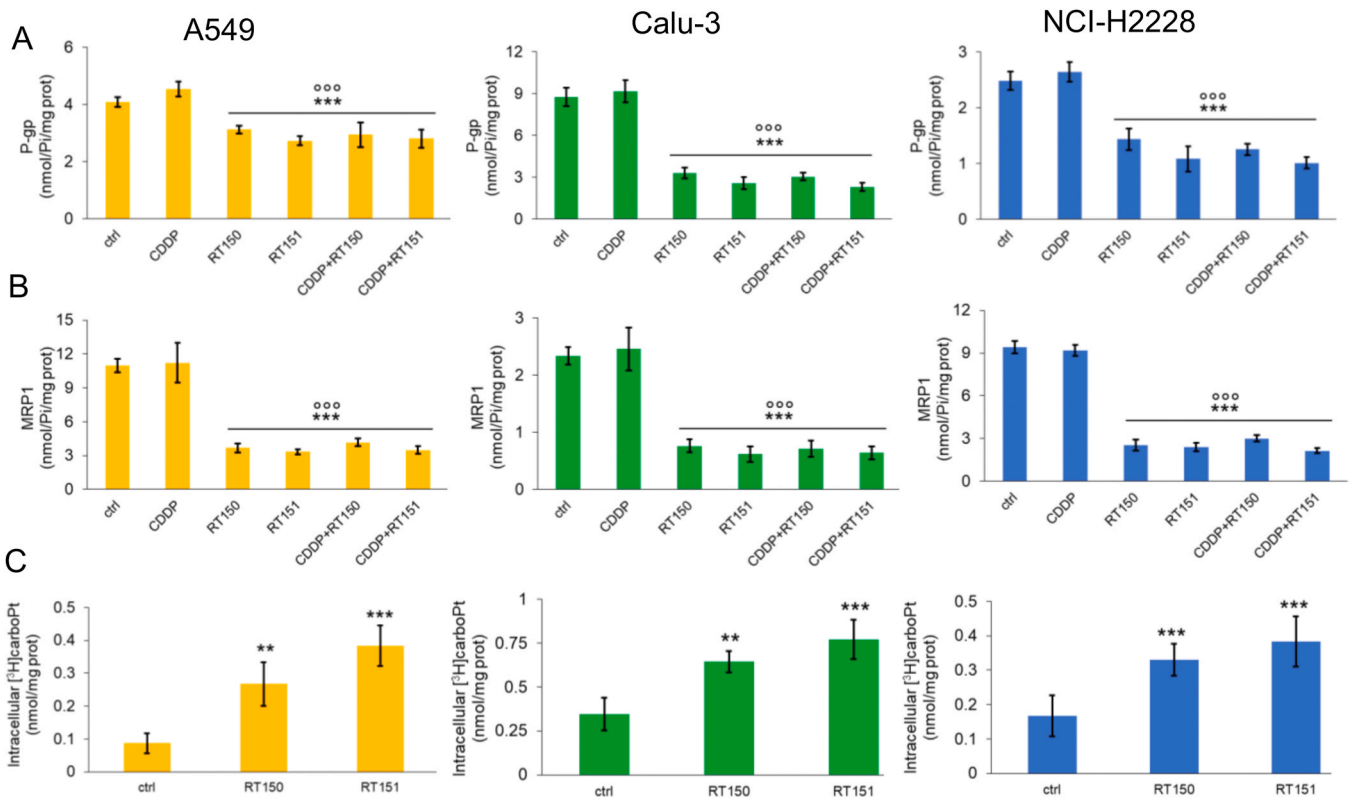

Fig. 2. RT150 and RT151 increased intracellular retention of carboplatin in resistant non-small cell lung cancer lines. **A-B.** Human non-small cell lung cancer A549, Calu-3, and NCI-H2228 cells were incubated for 3 h with fresh medium (ctrl), 50 μM cisplatin (CDDP), 0.1 μM **RT150** or **RT151**, individually or in combination. ATPase activity of ABCB1/P-gp and ABCC1/MRP1 was measured spectrophotometrically in technical duplicates. Data are expressed as mean ± SD (n=3 independent experiments). ***p<0.001 vs ctrl; °°°p<0.001 vs CDDP alone. **C.** Cells were labeled 3 h with μCi [^{14}C]-carboplatin, alone (ctrl) or with 0.1 μM **RT150** or **RT151**. The concentration of carboplatin was measured by liquid scintillation in duplicates. Data are expressed as mean ± SD (n=3 independent experiments). **p < 0.01, ***p < 0.001 vs ctrl.

used in the molecular docking protocol where compounds **RT150** and **RT151** were docked in the large central cavity of the protein. From the docking solutions, three different pockets, which were numbered according to their depth inside the protein cavity, were detected (Fig. 3C). The binding energies showed that the compounds were better ligands for the human rather than the *Bos taurus* form and that pocket 3 in the human structures has consistently higher energies (Table 1). This pocket is positioned on a region usually occupied by a loop/linker connecting two structured domains, which is missing in the *Bos taurus* X-ray and our human models, therefore, there is a large uncertainty related to its size and correct location. Our data also shows that the AlphaFold2 structure does not correctly accommodate the ligands in pocket 1, most likely due to its closed cavity. However, in the more realistic open structure, obtained from homology modeling, this deeper pocket becomes more stable indicating a downhill energy landscape for the binding of our ligands. The energy differences between **RT150** and **RT151** were negligible, probably due to the high similarity in their structures and the fact that quite different configurations in each pocket (Fig. 3D) still lead to very similar energy values.

The best binding modes for each of the three pockets represented in Fig. 3**C** are shown. The three structures used were the X-ray from *Bos taurus*, the human homology model obtained from the bovine structure, and the human structure available in the AlphaFold Protein Structure Database [43]. The pockets with the lowest energy values for each compound are identified with grey-shaded cells. All energy values are in kcal/mol.

In NCI-H2228 cells, expressing both P-gp and MRP1 [52], the decrease in protein pump activity was not the consequence of a low transcription rate (9). Though some P-gp inhibitors increase ubiquitination and internalization of the transporters [53], the ruthenium derivatives did not increase proteins' ubiquitination (9), nor change the amount of P-gp and MRP1 detected in cell lysates (9) or on the cell surface (9).

In constitutively CDDP-resistant cell lines A549, Calu-3 and NCI-H2228, the combination of **RT150** or **RT151** with CDDP markedly reduced the IC_{50} compared to CDDP alone (Table 1; 9) and the CI index indicated a strong synergistic effect (Table 1). In CDDP-sensitive NCI-H1650 and NCI-H1975 cell lines, characterized by very low levels of P-gp and MRP1 [52], **RT150** and **RT151** had no effects or displayed moderate antagonistic activity towards CDDP. However, in NCI-H1650/CDDP and NCI-H1975/CDDP sublines that represent models of acquired resistance, both **RT150** and **RT151** markedly decreased the CDDP IC_{50} value and showed a synergistic effect similar to that observed in constitutively CDDP-resistant cell lines (Table 2; 9).

Cells were incubated for 72 h. Cell viability was evaluated by the MTT assay. CI was calculated according to the Chou-Talalay method. Data are expressed as mean ± SD (n=3 independent experiments).

3.2. *Biocompatibility and toxicological assays of RT150 and RT151 on non-transformed cells*

Determination of the hemolytic potential of new molecules is an important step in their preliminary safety evaluation. The biocompatibility of **RT150** and **RT151** (1–100 μM) was investigated by assessing their capability to cause hemolysis (Fig. 4). Negative and positive control samples showed hemolysis values < 2 % and 100 %, respectively, supporting the appropriateness of the experiment. **RT150** and **RT151** showed good hemocompatibility up to 10 μM with a calculated hemolytic index < 5 % (considered non-hemolytic, according to ASTM F 756–00, 2004; [54]). At 100 μM, both compounds caused hemolysis,

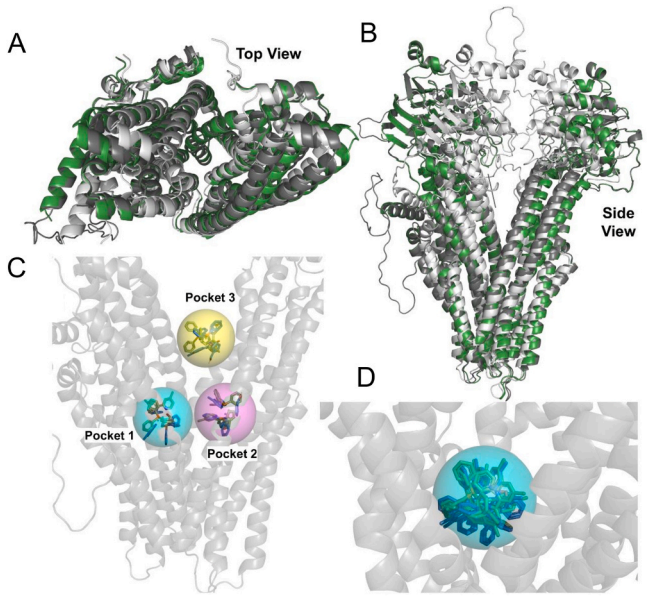

Fig. 3. Superposition of the three MRP1 structures used in this work and the docking solutions that identified the three binding pockets of the protein. **A–B**. The three MRP1 structures shown are the X-ray from *Bos taurus* (green), the human homology model obtained from the *Bos taurus* structure (dark grey), and the human structure available in the AlphaFold database (light grey). **C**. The best molecular docking solutions for **RT150** and **RT151** for each pocket of the homology model are shown. **D**. The five best solutions of both compounds in pocket 1 of the homology model are shown to illustrate their configurational variability.

which was more pronounced with **RT150** than **RT151** (97 % *vs* 47 %, $p<0.05$). However, these concentrations can hardly be obtained in *in vivo* experiments.

To test the toxicity of **RT150** and **RT151** on non-transformed cells, their concentration- and time-dependent effect were evaluated in human dermal adult fibroblasts HDFa, human small airway epithelial cells HSAEC, rat cardiomyoblasts H9c2 cells, and endothelial EA.hy926 cells. The IC_{50} values were inversely correlated to the incubation time (Table 3, 9), and even after 72 h were > 2 μM, a concentration 20-fold higher than that effectively rescuing CDDP resistance and unlikely to be reached *in vivo*. **RT151** and **RT150** showed comparable potency at all the time points considered.

Cells were incubated for 24, 48 or 72 h with either compounds. Cell viability was evaluated by the MTT assay. Data are expressed as mean ± SD (n=3 independent experiments).

EA.hy926 cells were the most sensitive cell line, followed by H9c2 cells. However, both compounds induced evident apoptosis in H9c2 cells, though only at concentrations > 10 μM, in a time-independent manner (9).

Table 2
IC_{50} values (μM) of CDDP, alone and combined with RT150 or RT151, in non-small cell lung cancer cells and corresponding Combination Indexes (CI).

Cell line	IC_{50} CDDP	IC_{50} CDPP+RT150	CI	IC_{50} CDPP+RT151	CI
A549	>100	9.94 ± 3.45	0.119	9.85 ± 2.11	0.063
Calu−3	92.33 ± 11.25	4.97 ± 1.67	0.009	4.78 ± 2.34	0.038
NCI-H2228	>100	3.16 ± 0.78	0.023	7.64 ± 0.98	0.064
NCI-H1650	4.90 ± 1.02	5.05 ± 0.98	1.32	5.00 ± 1.03	1.71
NCI-H1650/ CDDP	54.80 ± 3.45	24.42 ± 2.87	0.129	10.01 ± 1.01	0.188
NCI-H1975	1.84 ± 1.05	4.93 ± 0.65	1.49	5.37 ± 0.78	1.383
NCI-H1975/ CDDP	89.21 ± 10.89	5.04 ± 1.21	0.041	4.93 ± 0.76	0.046

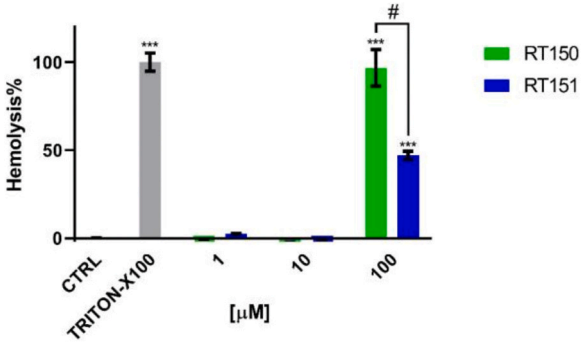

Fig. 4. Hemolytic potential. **RT150** and **RT151** were tested at 1 μM, 10 μM, and 100 μM, evaluated at pH 7.4, 6.8, 6.2, or 5.6, in technical duplicates. Data are means ± SD (n = 6 independent experiments). Triton-X100 (2 % v/v) was included as a positive control of hemolysis inducer. ***p < 0.001 vs control (ctrl) group, one-way Anova with Dunnet's post-test; #p<0.05, **RT150** vs. **RT151**, multiple t-tests with Holm-Sidak correction.

Table 3
IC_{50} values (μM) of RT150- or RT151-treated non-transformed cells.

Cell line	Time	RT150	RT151
HdFa	24 h	>100	79.9 ± 7.9
HdFa	48 h	30.2 ± 9.7	38.4 ± 14.9
HdFa	72 h	16.8 ± 3.0	13.8 ± 1.8
HSAEC	24 h	>100	>100
HSAEC	48 h	43.4 ± 8.7	39.6 ± 5.8
HSAEC	72 h	29.4 ± 2.9	29.6 ± 1.0
H9c2	24 h	44.8 ± 33.5	49.9 ± 27.6
H9c2	48 h	52.0 ± 37.7	27.9 ± 3.3
H9c2	72 h	11.9 ± 0.6	16.5 ± 7.0
EA.hy926	24 h	10.1 ± 0.9	13.9 ± 3.9
EA.hy926	48 h	5.0 ± 1.3	3.5 ± 0.4
EA.hy926	72 h	4.3 ± 1.1	2.3 ± 0.3

Table 1
Molecular docking energies calculated with Autodock Vina for compounds RT150 and RT151 in the MRP1 protein.

Structure	*Pocket 1*		*Pocket 2*		*Pocket 3*	
	RT150	**RT151**	**RT150**	**RT151**	**RT150**	**RT151**
Bos Taurus (X-ray)	-7.5	-7.5	-6.7	-7.1	-6.7	-6.6
Human (Homology)	-8.3	-8.3	-7.7	-7.9	-7.0	-6.7
Human (AF2)	-7.2	-7.0	-9.3	-8.6	-6.6	-6.7

3.3. Vascular effects of RT150 and RT151

Ruthenium-derived compounds may be considered anti-angiogenic agents, due to their ability to decrease endothelial nitric oxide production from EA.hy926 cells [55]. Therefore, the effects of the ruthenium derivatives on EA.hy926 cell migration, which is considered a phenomenon key to vessel formation and repairment, were assessed. Both compounds significantly inhibited the migration of EA.hy926 cells at 8 h and 24 h compared to control conditions, **RT151** being effective already at 1 μM concentration (9).

To further characterize the safety profile of the compounds, the effects of **RT150** and **RT151** were assessed on *in vitro* electro- and pharmaco-mechanical coupling. In rings pre-contracted by 60 mM KCl, **RT150** and **RT151** caused a concentration-dependent relaxation with IC_{50} values of 0.39 ± 0.13 μM and 0.35 ± 0.15 μM, respectively (Fig. 5A). Similar results were obtained in rings pre-contracted by the α_1 adrenergic receptor agonist phenylephrine (IC_{50} values of 1.56 ± 0.95 μM and 0.71 ± 0.36 μM, respectively; Fig. 5B). As **RT150** and **RT151** were able to relax depolarized aorta rings, where contraction is elicited by extracellular Ca^{2+} influx through open $Ca_V1.2$ channels, their effects on the $Ca_V1.2$ channel function were assessed by recording $I_{Ba1.2}$ in isolated tail main artery myocytes. **RT150** and **RT151** inhibited the current, recorded with depolarizing steps to 10 mV from a V_h of −50 mV, in a concentration-dependent manner with IC_{50} values of 2.94 ± 2.12 μM and 0.66 ± 0.32 μM, respectively (Fig. 5C). Furthermore, as shown in Figs. 5D-E, 5 μM **RT150** and 1 μM **RT151** significantly inhibited the peak inward current of the current-voltage relationships, recorded at a V_h of −50 mV, in the range between −30 mV and 50 mV and −20 mV and 40 mV, respectively. Finally, **RT150** shifted the apparent maximum by 5 mV in the hyperpolarizing direction without, however, varying the threshold at about −40 mV.

3.4. Encapsulation of RT151 in Captisol® and stability in ultrapure water

The above *in vitro* evidence indicated **RT151** as the more effective chemosensitizer. However, to test its *in vivo* efficacy and safety, an appropriate chemical system is required to convert this high lipophilic, low molecular weight compound into a potentially deliverable pharmaceutical. Therefore, the ability of sulfobutyl ether β-cyclodextrin sodium salt (commercially available under the name of Captisol®) to increase the aqueous solubility of **RT151** was explored. Indeed, encapsulation of **RT151** into Captisol® effectively increased its water solubility up to 1.33 mg/mL without causing any changes to the compound structure, thus allowing its i.v. administration as an inclusion complex (**RT151**-Captisol®) without the need for any co-solvent. The absorption spectrum of **RT151** (see 9) pointed to a good stability profile over 4 weeks, with no apparent changes, thus indicating the absence of structural modifications of the compound over time under these conditions.

3.5. RT151 was effective against cisplatin-resistant non-small cell lung cancer xenografts

To identify the maximum tolerated dose in NSG mice, a dose escalation experiment was first performed treating mice for 5 weeks with 3, 6, and 10 mg/kg **RT151**. This range of doses was selected based on a previous study using ruthenium-cyclopentadienyl compounds as antitumor agents [56]. No deaths were detected in the group treated with 3 mg/kg **RT151**, while the groups treated with 6 and 10 mg/kg **RT151** recorded a death rate of 25 % (1 dead mouse out of 4) and 50 % (2 dead mouse out of 4) during the last week of treatment, respectively.

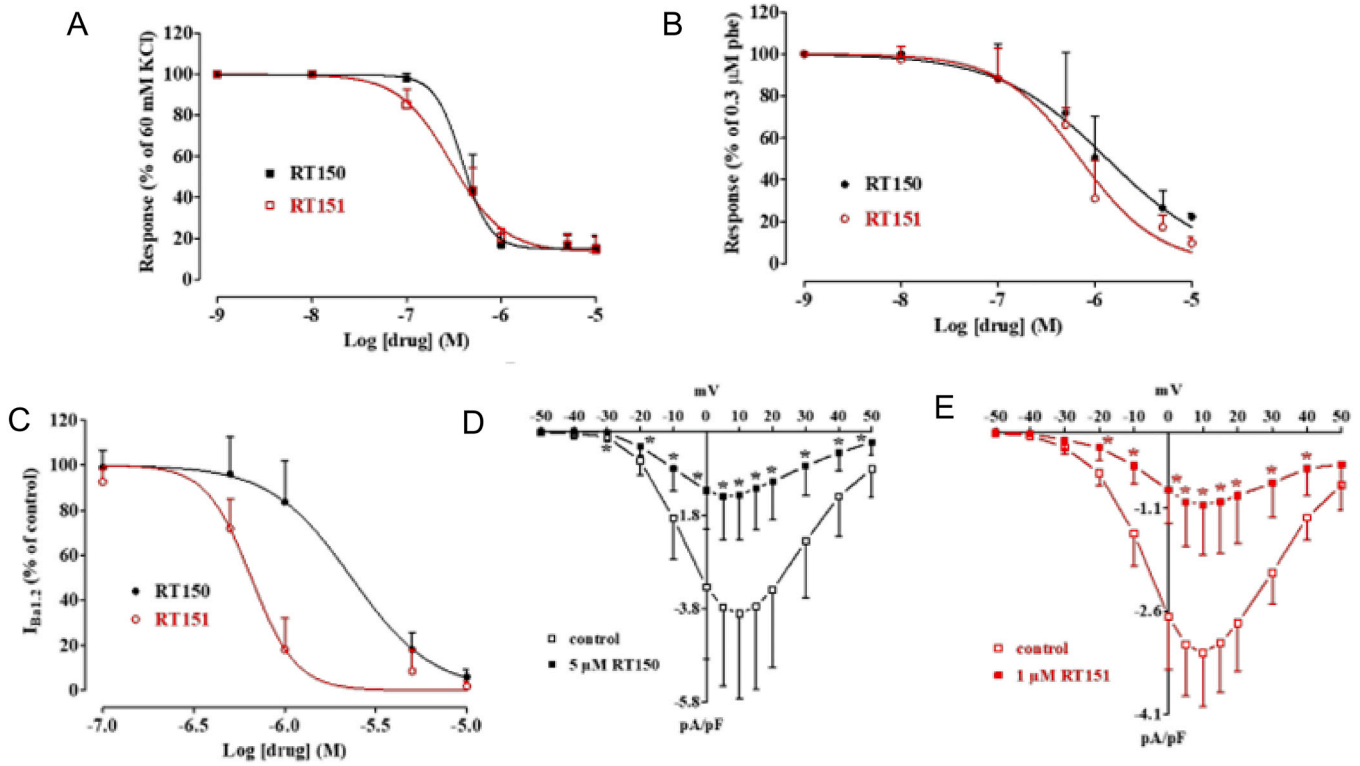

Fig. 5. RT150 and RT151 relax rat aorta rings and block rat tail artery myocytes $Ca_V1.2$ channels. **A-B.** Concentration-response curves for **RT150** and **RT151** on endothelium-denuded rat aorta rings pre-contracted by either (**A**) 60 mM KCl or (**B**) 0.3 μM phenylephrine. On the ordinate scale, the response is reported as a percentage of the initial tension induced by KCl or phenylephrine. Data are mean ± SD (n = 5 independent experiments for **A**, 6 independent experiments for **B**). **C.** Concentration-dependent effect of **RT150** and **RT151** at the peak of $I_{Ba1.2}$ trace recorded in rat tail artery myocytes. The curves show the best fit of the points. On the ordinate scale, current amplitude is reported as a percentage of that recorded before the addition of the drug. Data points are mean ± SD (n = 7 independent experiment). **D-E.** Effect of (**D**) **RT150** and (**E**) **RT151** on the current-voltage relationship, recorded from a V_h of −50 mV, constructed in the absence (control) or presence of either 5 μM **RT150** or 1 μM **RT151.** Data points are mean ± SD (n = 5 independent experiment). *p < 0.05 vs control.

Although no significant pathological alterations were observed in the liver, kidney, and spleen, *i.e.,* the organs involved in metabolism and sequestration by reticuloendothelial system cells (9), only the low (3 mg/kg) and medium (6 mg/kg) doses were assessed in the following experiments.

As shown in Fig. 6, CDDP did not significantly reduce tumor growth of A549 xenografts. This outcome was not surprising, given the well-known intrinsic drug resistance of the NSCLC model to CDDP [52] and other chemotherapeutic drugs [57]. Conversely, **RT151** decreased tumor growth in a dose-dependent manner, with reduction being greater when both doses of **RT151** were combined with CDDP (Fig. 6A). The marked anti-tumor effect of the highest dose of **RT151**, either alone or combined with CDDP, was paralleled by reduced intratumor proliferation and apoptosis, as indicated by Ki67 positive cells and by the increased activity of caspase 3, respectively (Fig. 6B).

3.6. RT151 bioaccumulation in mice bearing non-small cell lung cancer xenografts

The ruthenium and platinum content in tumors, kidneys, lungs, liver, and spleen was measured by ICP-MS analysis to quantify drug bioaccumulation and *in vivo* ability to target A549 tumors after systemic administration (Fig. 7A-B). A direct correlation between tumor size and platinum and ruthenium accumulation was found, the latter being higher when CDDP or ruthenium were administered alone (Fig. 7C). A marked decrease was observed in platinum accumulation when co-administered with **RT151**, in particular with the 6 mg/kg **RT151** + CDDP regimen, where the tumors were much smaller. Platinum was found in high amounts also in the liver and kidneys, whereas the lungs and spleen showed concentrations lower than 0.1 μg/g dried samples. Differently, ruthenium was mainly found in highly perfused organs, such as the spleen and lungs, with lower concentrations being found in the liver and kidneys.

3.7. In vivo safety of RT151 in non-small cell lung cancer xenografts

Several parameters were monitored to assess the biosafety of **RT151** *in vivo*. First, the weights of the animals did not significantly vary among all treatment groups (Fig. 8A). Second, *post-mortem* analyses did not show significant alterations in the histological architecture of the liver, kidneys and spleen, either when the agents were used alone or in combination with CDDP, at both dosages (Fig. 8B).

Finally, ruthenium derivatives safety was assessed also through the analysis of the hematochemical parameters at the end of the study (Table 4). No signs of myelotoxicity were detected: in fact, the number of red blood cells, white blood cells, and platelets as well as the concentration of hemoglobin were not modified by the different treatments. Though scarcely accumulated in the liver, 6 mg/kg **RT151** increased the level of alanine aminotransferase without, however, affecting those of lactic dehydrogenase, aspartate aminotransferase, and alkaline phosphatase, thus indicating limited hepatotoxicity. Furthermore, no differences were observed in the level of alanine aminotransferase between animals treated with 6 mg/kg **RT151**, alone or in combination with CDDP, suggesting that the accumulation of the drug in the liver did not

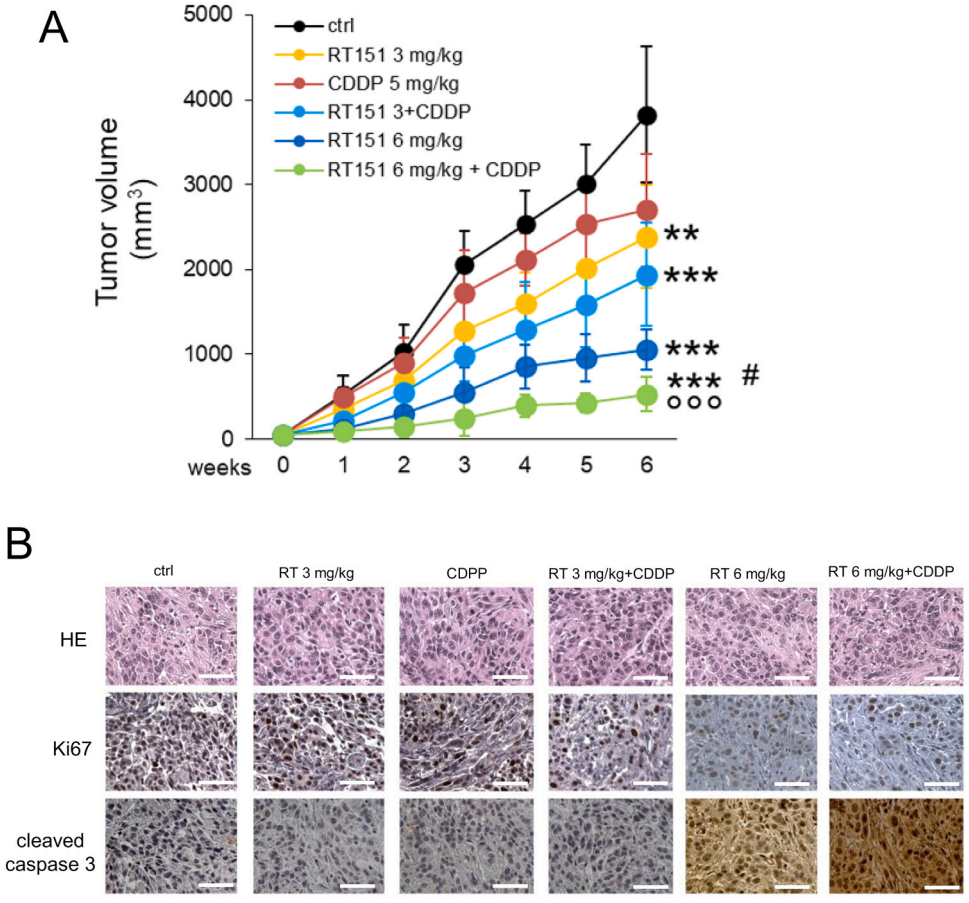

Fig. 6. Efficacy of RT151 against A549 xenografts. NSG mice bearing A549 tumors of 50 mm^3 volume were randomized (5 mice/group) and treated for 6 weeks (once/week) intravenously, as follows: 0.1 mL Captisol® (ctrl); 5 mg/kg cisplatin (CDDP); 3 mg/kg **RT151**; 5 mg/kg CDDP + 3 mg/kg **RT151**; 6 mg/kg **RT151**; 5 mg/kg CDDP + 3 mg/kg **RT151**. **A.** Tumor growth monitored with caliper. Data are mean volumes ± SD. **p < 0.01, ***p < 0.001 vs ctrl group; °°° p < 0.001 vs CDDP alone; #p < 0.05 6 mg/kg **RT151** or 5 mg/kg CDDP + 6 mg/kg **RT151** vs 3 mg/kg **RT151** or 5 mg/kg CDDP + 3 mg/kg **RT151** (week 6). **B.** Representative tumor sections stained with hematoxylin-eosin, Ki67, and cleaved caspase 3. Ocular: 10x; objective: 20x. Bar: 50 μm.

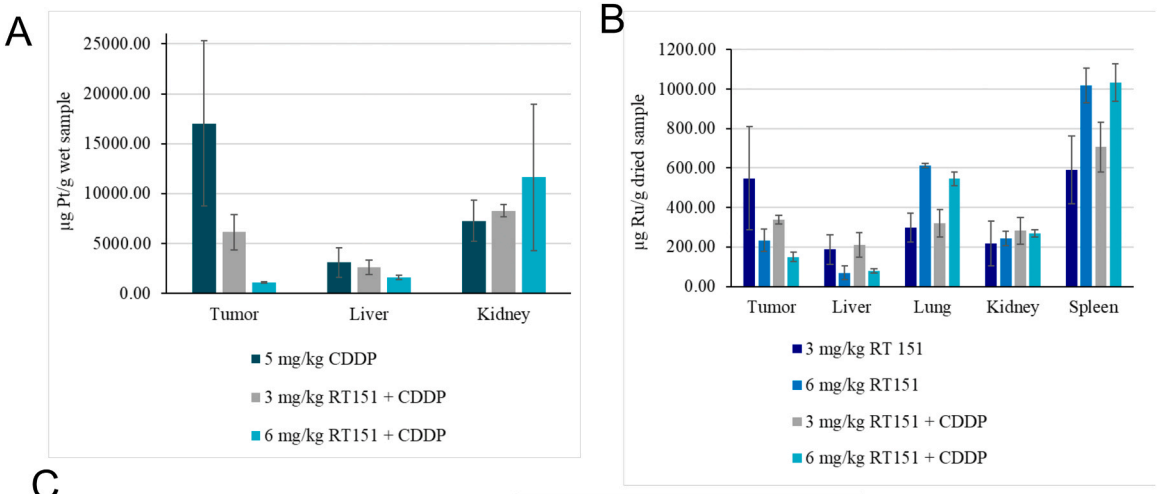

C

					Combination Treatment	
	Control	CDDP (5 mg/kg)	**RT151** (3 mg/kg)	**RT151** (6 mg/kg)	**RT151** (3 mg/kg) + CDDP (5 mg/kg)	**RT151** (6 mg/kg) + CDDP (5 mg/kg)
Volume (mm^3)	3825	2696	2385	1051	1939	528
Tumour reduction (%)	-	30	38	73	49	86
µg Ru/g dry sample)	-	-	547	234	339	150
µg Pt/g dry sample)	-	17026	-	-	6153	1103

Fig. 7. Biodistribution of RT151 and CDDP in mice tumors and main organs. **A-B.** Platinum and ruthenium content in mice tumors and main organs after treatment with CDDP (5 mg/kg), **RT151** (3 or 6 mg/kg), and CDDP+**RT151** (3 or 6 mg/kg, respectively) for six weeks. Data are means ± SD (n = 3) and results are expressed as µg Ru and Pt/g of dry organ or tissue. **C.** Volume (in mm^3) and tumor volume reduction (in %) after treatment with either CDDP or **RT151** and combination treatment, as well as Ru and Pt content in tumors.

cause additional damage. In line with the distribution and with the expected nephrotoxicity, CDDP increased the level of creatinine, a marker of kidney function impairment. However, **RT151** did not worsen such damage, even when the dose of 6 mg/kg was administered in combination with CDDP, *i.e.*, the association that provided the maximal antitumor efficacy. Finally, none of the treatments induced cardiac toxicity as indicated by the lack of changes in the levels of creatine phosphate kinase and troponin cardiac isoform.

4. Discussion

RT150 and **RT151** compounds had previously shown a significantly lower IC_{50} value than CDDP in resistant NSCLC cell lines, coupled with the ability to inhibit P-gp [21]. In the present study, the mechanism of action of the compounds was analyzed in more detail, using the concentration necessary to inhibit P-gp and analyzing their effects when used alone or in combination with CDDP. **RT150** and **RT151** induced oxidative stress in all the CDDP-resistant NSCLC cell lines analyzed, eliciting oxidative DNA damage and, consequently, cell cycle arrest. When combined with CDDP, which damages DNA in sensitive cells, **RT150** and **RT151** rescued CDDP efficacy even in resistant cells.

Since the cytotoxic effects of CDDP depend on the drug's intracellular concentration, we hypothesized that **RT150** and **RT151** increased the retention of CDDP, a substrate of ABCB1/P-gp and ABCC1/MRP1. An experimental approach combining computational modeling and site-directed mutagenesis on the *ABCB1/mdr1* gene, has already demonstrated that both **RT150** and **RT151** bind specific residues of the R-site of P-gp, localized at the plasma-membrane/protein interface, which is critical for entry and/or export of drugs. By strongly binding to this site, **RT150** and **RT151** become inhibitors of P-gp [21]. A similar mechanism might occur in the case of MRP1. In the present work, by comparing the docking of **RT150** and **RT151** to MRP1 of *Bos taurus*, which has the X-ray structure with the highest homology to human MRP1, and to two models of human MRP1 (with the internal cavity more closed or more open), we predicted that the compounds bind preferably to pocket 1, which is located deep inside human MRP1's central cavity. We hypothesize a process not too different from P-gp [21] where ligands can bind transient pockets step-wisely and move on a downhill energy landscape until they reach the deeper and more stable binding mode. From this pocket, substrates can be more easily exported, while inhibitors can stay longer and interfere with the normal functioning of the protein. These results are consistent with the hypothesis that **RT150** and **RT151** inhibit the catalytic activity of ABC transporters by interacting with key residues in specific pockets involved in drug entry or efflux. Specifically, as demonstrated by the intracellular accumulation of carboplatin, they inhibited the efflux of the drug, increasing its cytotoxic activity.

Intriguingly, **RT150** and **RT151** displayed a synergistic effect with CDDP only in drug-resistant cell lines, characterized by either constitutive or acquired resistance, and sharing a high expression of P-gp and MRP1. These results suggest that the inhibition of drug efflux exerted by **RT150** and **RT151** is the *primum movens* contributing to the increased retention of CDDP and provides an explanation for the enhanced cytotoxic effects of the association **RT150** or **RT151** and CDDP, capable of reversing drug resistance in NSCLC cells with constitutive or acquired resistance, which mimic the pathological condition occurring in cancer patients developing chemoresistance during therapy.

The peculiarity of **RT150** or **RT151**, killing preferentially CDDP-resistant cancer cell lines, represents a key feature for the safety of healthy tissues. This is further supported by the lack of cytotoxicity on primary non-transformed cells of different origins and by the good hemocompatibility, at least at concentrations conceivably reached during therapy. These results agree with other studies where the biphosphinic ruthenium complex cis-$[Ru(dppb)(bqdi)Cl_2]^{2+}$ showed

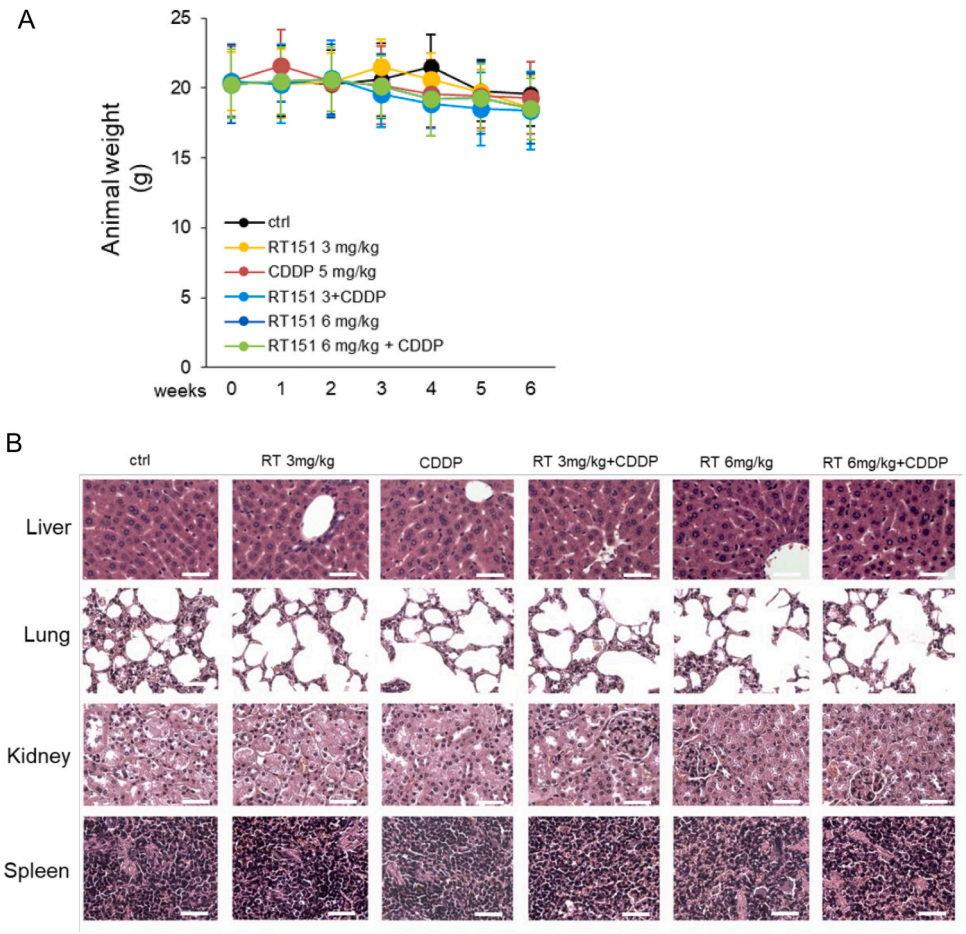

Fig. 8. Body weight and post-mortem organ pathology of CDDP and RT151 treated mice. NSG mice bearing A549 tumors of 50 mm^3 volume were randomized (5 mice/group) and treated for 6 weeks (once/week) intravenously, as follows: 0.1 mL Captisol® (ctrl); 5 mg/kg cisplatin (CDDP); 3 mg/kg **RT151**; 5 mg/kg CDDP + 3 mg/kg **RT151**; 6 mg/kg **RT151**; 5 mg/kg CDDP + 3 mg/kg **RT151**. **A.** Mice body weight was monitored once/week during the treatment. Data are means ± SD. **B.** Representative hematoxylin-eosin stains of liver, lung, kidney, and spleen sections. Ocular: 10x; objective: 20x (liver, lung, and kidney); 10x (spleen). Bar: 50 μm.

good hemocompatibility at concentrations up to 100 μg/mL [58]. Taken together, these data indicate that both ruthenium derivatives possess a favorable safety profile, toxicity emerging only at concentrations well above those expected *in vivo*. Hence, they might represent effective anti-tumor agents devoid of significant side effects. Moreover, the anti-migratory effects of **RT150** and **RT151** on human endothelial cells highlighted their potential to act as anti-angiogenic agents in cancer therapy. The electro- and pharmaco-mechanical coupling assays proved that both derivatives might exert vasorelaxant activity, consistent with a previous report demonstrating that nitrosyl-ruthenium-containing compounds show antioxidant and vasorelaxant properties on rat aorta ring [59]. The electrophysiology experiments pointed to $Ca_V1.2$ channel blockade as a mechanism responsible for **RT150** and **RT151** vasoactivity. However, while high KCl-induced contraction is dependent essentially on $Ca_V1.2$ channel opening, this pathway only partially contributes to phenylephrine-induced contraction, where cytoplasmic Ca^{2+} increase occurs also with the contribution of IP_3-sensitive stores and extracellular influx through receptor- and store-operated Ca^{2+} channels. Therefore, it is conceivable to hypothesize that both compounds are capable of targeting mechanisms regulating smooth muscle tone other than $Ca_V1.2$ channels. Further experiments, going beyond the scope of the present investigation, are needed to clarify this point.

Taken together, the above results suggest that **RT151** has a favorable "therapeutic window", is more effective in overcoming CDDP resistance, and shows a slightly better anti-tumor activity coupled with a good anti-migration effect *in vitro* than **RT150**, along with possessing a comparable and valuable safety profile. Additionally, plasma and metabolic stability data support the choice of **RT151** as the best promising hit compound [60].

In vivo results confirmed that **RT151** is capable to act as a potent synergistic agent with CDDP against resistant tumors, where the reduced intratumor proliferation and the high level of apoptosis reproduced cell proliferation inhibition and apoptosis induction observed *in vitro*. Notably, considering the effects of other metal-based compounds on A549 xenografts [14–19], **RT151** emerged to possess the best tumor growth inhibitory activity and to be the only one endowed with a potent synergistic outcome in association with CDDP. Moreover, this is the first study performed on a resistant lung cancer model providing direct evidence of an inverse correlation between P-gp/MRP1 expression and compound activity. Remarkably, other compounds developed by this research group as novel ABC pump inhibitors have shown a consistent correlation between *in vitro* and *in vivo* data. **LCR134**, $[Ru(\eta^5\text{-}C_5H_5)(4,4'\text{-dibiotin ester-}2,2'\text{-bipyridine})(PPh_3)]^+$, for example, inhibits the multidrug-resistant P-gp transporter across species [22] supporting its pharmacological translatability: indeed, the transporter was inhibited in an *in vivo* zebrafish model at low doses, which could limit the off-target effects of the chemotherapeutic.

An *in vitro-in vivo* alignment was also obtained for the toxicological parameters: despite a preferential accumulation of ruthenium in the spleen and lungs, no signs of significant systemic toxicity were detected, thus suggesting a reliable safety profile.

Table 4
Hematochemical parameters of the mice.

Parameter	ctrl	CDDP	**RT151** 3 mg/kg	**RT151** 3 mg/kg+CDDP	**RT151** 6 mg/kg	**RT151** 6 mg/kg+CDDP
RBC ($\times 10^6$/μL)	14.20 ± 2.14	14.05 ± 1.08	13.87 ± 2.14	13.58 ± 2.07	14.05 ± 1.47	13.69 ± 1.52
Hb (g/dL)	14.19 ± 2.36	12.45 ± 2.11	12.39 ± 2.58	12.48 ± 2.47	12.58 ± 1.96	12.58 ± 1.52
WBC ($\times 10^3$/μL)	15.29 ± 2.82	14.78 ± 1.82	14.58 ± 3.24	16.35 ± 1.87	14.69 ± 1.74	17.25 ± 3.41
PLT ($\times 10^3$/μL)	827 ± 315	775 ± 201	689 ± 228	664 ± 214	678 ± 308	608 ± 143
LDH (U/L)	7058 ± 524	6245 ± 328	6245 ± 505	6852 ± 508	7152 ± 369	7452 ± 531
AST (U/L)	158 ± 46	142 ± 39	118 ± 52	179 ± 63	205 ± 39	228 ± 38
ALT (U/L)	44 ± 9	58 ± 11	52 ± 10	62 ± 8	75 ± 6*	73 ± 8*
AP (U/L)	108 ± 14	158 ± 33	115 ± 28	128 ± 39	169 ± 12	175 ± 12
Creatinine (mg/L)	0.073 ± 0.011	0.091 ± 0.009*	0.079 ± 0.008	0.094 ± 0.008*	0.082 ± 0.025	0.096 ± 0.008*
CPK (U/L)	285 ± 86	306 ± 54	324 ± 71	277 ± 17	271 ± 39	298 ± 81
c-TNT (ng/mL)	0.011 ± 0.005	0.010 ± 0.005	0.012 ± 0.006	0.012 ± 0.006	0.015 ± 0.006	0.014 ± 0.006

Animals were treated as reported in the Materials and methods section. The hematochemical parameters were measured in blood samples collected immediately after euthanasia. Data are means ± SD (5 mice/group). *$p < 0.05$ vs ctrl group. RBC: red blood cells; WBC: white blood cells; Hb: hemoglobin; PLT: platelets; LDH: lactate dehydrogenase; AST: aspartate aminotransferase; ALT: alanine aminotransferase; AP: alkaline phosphatase; CPK: creatine phosphokinase; c-TNT: cardiac troponin.

5. Conclusions

Overall, this work suggests that the ruthenium derivatives **RT150** and **RT151** can restore the sensitivity to CDDP in CDDP-resistant cell lines and show good biocompatibility and modest *in vitro* cardiotoxicity in non-transformed cells up to 5 μM concentration. **RT151** performed slightly better than the analogue **RT150** in overcoming CDDP resistance in three NSCLC cell lines, regardless of their genetic background, and as an anti-migratory agent. *In vivo*, **RT151** combined with CDDP showed a good balance between high anti-tumor efficacy and limited toxicity at the lowest dose assessed and, at the highest dose, allowed the achievement of the maximal therapeutic effect (86 % tumor reduction) without exacerbating the toxic effects of CDDP. As CDDP still represents the first-line chemotherapeutic treatment of NSCLC, its association with **RT151** can represent an alternative, effective, and relatively safe strategy for the treatment of CDDP-resistant tumors.

CRediT authorship contribution statement

Fabio Fusi: Formal analysis. **Virginia Tzankova:** Writing – review & editing, Formal analysis, Data curation. **Yordan Yordanov:** Writing – review & editing, Investigation, Data curation. **Miguel Machuqueiro:** Writing – review & editing, Formal analysis. **Simona Saponara:** Writing – original draft, Formal analysis, Conceptualization. **Andreia Valente:** Writing – review & editing, Supervision, Resources, Formal analysis, Conceptualization. **Chiara Riganti:** Writing – review & editing, Supervision, Resources, Formal analysis, Conceptualization. **Iris C. Salaroglio:** Writing – original draft, Investigation, Formal analysis. **Denitsa Stefanova:** Investigation, Formal analysis. **Ricardo G. Teixeira:** Writing – original draft, Resources. **Nuno F.B. Oliveira:** Formal analysis, Data curation. **Amer Ahmed:** Investigation.

Fundings

This work was financed by the Portuguese Foundation for Science and Technology (Fundação para a Ciência e Tecnologia, FCT) within the scope of Projects UIDB/00100/2020 (Centro de Química Estrutural; 10.54499/UIDP/00100/2020), UIDB/04046/2020 (BioISI; 10.54499/UIDB/04046/2020), LA/P/0056/2020 (Instituto de Ciências Moleculares; 10.54499/LA/P/0056/2020) and PTDC/QUI-QIN/28662/2017. R.G. Teixeira thanks FCT for his Ph.D. Grant (SFRH/BD/135830/2018 and COVID/BD/153190/2023). A. Valente and M. Machuqueiro acknowledge the CEECIND 2017 Initiative (CEECCIND/01974/2017–10.54499/CEECIND/01974/2017/CP1387/CT0014 and CEECIND/02300/2017–10.54499/CEECIND/02300/2017/CP1387/CT0031, respectively). N.F.B. Oliveira acknowledges FCT grant 2021.06409.BD and I.C. Salaroglio acknowledges the PNRR - PNC - D3 4 HEALTH grant (Italy). C. Riganti thanks the Associazione Italiana per la Ricerca sul Cancro (AIRC; grants IG21408, IG29250). We acknowledge the National Science Fund of Bulgaria (grant KP-06-COST/21/2023 to V. Tzankova, D. Stefanova, and Y. Yordanov). The COST Action 17104 STRATAGEM (European Cooperation in Science and Technology) is also gratefully acknowledged.

Supplemental materials

Figure S1: effects of **RT150** and **RT151** on P-gp and MRP1 expression; Figure S2: effects of **RT150** and **RT151** on the viability of non-small cell lung cancer cells; Figure S3: effects of **RT150** and **RT151** on the viability of non-transformed cells; Figure S4: effects of **RT150** and **RT151** on apoptosis of cardiomyoblast cells; Figure S5: effects of **RT150** and **RT151** on endothelial cell migration; Figure S6: stability studies of **RT151**-Captisol inclusion complex in water; Figure S7: *post-mortem* pathology analysis of liver, kidney, and spleen in mice treated with increasing doses of **RT151**.

Declaration of Competing Interest

The Authors declare that they have not conflicts of interest. The Authors declare that they do not have used any artificial intelligence-based tools during the writing process.

Data availability

Data will be made available on request.

References

[1] World Cancer Research Fund International, Lung Cancer Statistics: https://www.wcrf.org/cancer-trends/lung-cancer-statistics/ (accessed 15 March 2024).
[2] J. Zhou, Y. Kang, L. Chen, H. Wang, J. Liu, S. Zeng, L. Yu, The drug resistance mechanisms of five platinum-based antitumor agents, Front. Pharmacol. 11 (2020) 1–17, https://doi.org/10.3389/fphar.2020.00343.
[3] L. Galluzzi, L. Senovilla, I. Vitale, J. Michels, I. Martins, O. Kepp, M. Castedo, G. Kroemer, Molecular mechanisms of cisplatin resistance, Oncogene 31 (2012) 1869–1883, https://doi.org/10.1038/onc.2011.384.
[4] S.Y. Lee, C.Y. Kim, T.G. Nam, Ruthenium complexes as anticancer agents: a brief history and perspectives, Drug Des. Dev. Ther. 14 (2020) 5375–5392, https://doi.org/10.2147/DDDT.S275007.
[5] S. Thota, D.A. Rodrigues, D.C. Crans, E.J. Barreiro, Ru(II) compounds: next-generation anticancer metallotherapeutics? J. Med. Chem. 61 (2018) 5805–5821, https://doi.org/10.1021/acs.jmedchem.7b01689.
[6] A. Valente, T.S. Morais, R.G. Teixeira, C.P. Matos, A.I. Tomaz, M.H. Garcia, Ruthenium and Iron Metallodrugs: New Inorganic and Organometallic Complexes as Prospective Anticancer Agents, Synthetic Inorganic Chemistry: New Perspectives, Elsevier, 2021, pp. 223–276.
[7] E. Alessio, Thirty years of the drug candidate NAMI-A and the myths in the field of ruthenium anticancer compounds: a personal perspective, Eur. J. Inorg. Chem. 2017 (2017) 1549–1560, https://doi.org/10.1002/ejic.201600986.
[8] R. Trondl, P. Heffeter, C.R. Kowol, M.A. Jakupec, W. Berger, B.K. Keppler, NKP-1339, the first ruthenium-based anticancer drug on the edge to clinical application, Chem. Sci. 5 (2014) 2925–2932, https://doi.org/10.1039/C3SC53243G.
[9] S. Monro, K.L. Colón, H. Yin, J. Roque, P. Konda, S. Gujar, R.P. Thummel, L. Lilge, C.G. Cameron, S.A. McFarland, Transition metal complexes and photodynamic

therapy from a tumor-centered approach: challenges, opportunities, and highlights from the development of TLD1433, Chem. Rev. 119 (2019) 797–828, https://doi.org/10.1021/acs.chemrev.8b00211.
[10] C. Holohan, S. Van Schaeybroeck, D.B. Longley, P.G. Johnston, Cancer drug resistance: an evolving paradigm, Nat. Rev. Cancer 13 (2013) 714–726, https://doi.org/10.1038/nrc3599.
[11] Q. Guo, H. Cao, X. Qi, H. Li, P. Ye, Z. Wang, D. Wang, M. Sun, Research progress in reversal of tumor multi-drug resistance via natural products, Anticancer. Agents Med. Chem. 17 (2017) 1466–1476, https://doi.org/10.2174/1871520617666171016105704.
[12] A. Valente, A. Podolski-Renić, I. Poetsch, N. Filipović, Ó. López, I. Turel, P. Heffeter, Metal- and metalloid-based compounds to target and reverse cancer multidrug resistance, Drug Resist. Updat. 58 (2021) 100778, https://doi.org/10.1016/j.drup.2021.100778.
[13] C.A. Vock, W.H. Ang, C. Scolaro, A.D. Phillips, L. Lagopoulos, L. Juillerat-Jeanneret, G. Sava, R. Scopelliti, P.J. Dyson, Development of ruthenium antitumor drugs that overcome multidrug resistance mechanisms, J. Med. Chem. 50 (2007) 2166–2175, https://doi.org/10.1021/jm070039f.
[14] L. Chen, G. Li, F. Peng, X. Jie, G. Dongye, K. Cai, R. Feng, B. Li, Q. Zeng, K. Lun, J. Chen, B. Xu, The induction of autophagy against mitochondria-mediated apoptosis in lung cancer cells by a ruthenium (II) imidazole complex, Oncotarget 7 (2016) 80716–80734, https://doi.org/10.18632/oncotarget.13032.
[15] V.H.S. Van Rixel, V. Ramu, A.B. Auyeung, N. Beztsinna, D.Y. Leger, L.N. Lameijer, S.T. Hilt, S.E. Le Dévédec, T. Yildiz, T. Betancourt, M.B. Gildner, T.W. Hudnall, V. Sol, B. Liagre, A. Kornienko, S. Bonnet, Photo-uncaging of a microtubule-targeted rigidin analogue in hypoxic cancer cells and in a xenograft mouse model, J. Am. Chem. Soc. 141 (2019) 18444–18454, https://doi.org/10.1021/jacs.9b07225.
[16] X. Li, Q. Huang, H. Long, P. Zhang, H. Su, J. Liu, A New Gold(I) Complex-Au(PPh3)PT is a deubiquitinase inhibitor and inhibits tumor growth, EBioMedicine 39 (2019) 159–172, https://doi.org/10.1016/j.ebiom.2018.11.047.
[17] L. He, K.N. Wang, Y. Zheng, J.J. Cao, M.F. Zhang, C.P. Tan, L.N. Ji, Z.W. Mao, Cyclometalated Iridium(Iii) complexes induce mitochondria-derived paraptotic cell death and inhibit tumor growth: in vivo, Dalt. Trans. 47 (2018) 6942–6953, https://doi.org/10.1039/c8dt00783g.
[18] Y.T. Chen, S.N. Zhang, Z.F. Wang, Q.M. Wei, S.H. Zhang, Discovery of Thirteen Cobalt(Ii) and Copper(Ii) salicylaldehyde schiff base complexes that induce apoptosis and autophagy in human lung adenocarcinoma A549/DDP cells and that can overcome cisplatin resistance in vitro and in vivo, Dalt. Trans. 51 (2022) 4068–4078, https://doi.org/10.1039/d1dt03749h.
[19] D. Mariani, Z. Ghasemishahrestani, W. Freitas, P. Pezzuto, A.C. Costa-da-Silva, A. Tanuri, M.M. Kanashiro, C. Fernandes, A. Horn, M.D. Pereira, Antitumoral synergism between a copper(II) complex and cisplatin improves in vitro and in vivo anticancer activity against melanoma, lung and breast cancer cells, Biochim. Biophys. Acta Gen. Subj. 1865 (2021) 129963, https://doi.org/10.1016/j.bbagen.2021.129963.
[20] R.G. Teixeira, D.C. Belisario, X. Fontrodona, I. Romero, A.I. Tomaz, M.H. Garcia, C. Riganti, A. Valente, Unprecedented collateral sensitivity for cisplatin-resistant lung cancer cells presented by new ruthenium organometallic compounds, Inorg. Chem. Front. 8 (2021) 1983–1996, https://doi.org/10.1039/D0QI01344G.
[21] R.G. Teixeira, I.C. Salaroglio, N.F.B. Oliveira, J.G.N. Sequeira, X. Fontrodona, I. Romero, M. Machuqueiro, A.I. Tomaz, M.H. Garcia, C. Riganti, A. Valente, Fighting multidrug resistance with ruthenium−cyclopentadienyl compounds: unveiling the mechanism of P-gp inhibition, J. Med. Chem. 66 (2023) 14080–14094, https://doi.org/10.1021/acs.jmedchem.3c01120.
[22] L. Côrte-Real, B. Karas, P. Gírio, A. Moreno, F. Avecilla, F. Marques, B.T. Buckley, K.R. Cooper, C. Doherty, P. Falson, M.H. Garcia, A. Valente, Unprecedented inhibition of P-Gp activity by a novel ruthenium-cyclopentadienyl compound bearing a bipyridine-biotin ligand, Eur. J. Med. Chem. 163 (2019) 853–863, https://doi.org/10.1016/j.ejmech.2018.12.022.
[23] M. Durante, M. Frosini, F. Fusi, A. Neri, C. Sticozzi, S. Saponara, Toxicology in vitro in vitro vascular toxicity of tariquidar, a potential tool for in vivo PET studies, Toxicol. Vitr 44 (2017) 241–247, https://doi.org/10.1016/j.tiv.2017.07.015.
[24] T. Mosmann, Rapid colorimetric assay for cellular growth and survival: application to proliferation and cytotoxicity assays, J. Immunol. Methods 65 (1983) 55–63, https://doi.org/10.1016/0022-1759(83)90303-4.
[25] J. López-García, M. Lehocký, P. Humpolícek, P. Sáha, P, Functional biomaterials HaCaT keratinocytes response on antimicrobial atelocollagen substrates: extent of cytotoxicity, cell viability and proliferation, J. Funct. Biomater. 5 (2014) 43–57, https://doi.org/10.3390/jfb5020043.
[26] G. Repetto, A. Peso, J.L. Zurita, Neutral red uptake assay for the estimation of cell viability/cytotoxicity, Nat. Protoc. 3 (2008) 1125–1131, https://doi.org/10.1038/nprot.2008.75.
[27] T.C. Chou, Drug combination studies and their synergy quantification using the Chou-Talalay method, Cancer Res 70 (2010) 440–446, https://doi.org/10.1158/0008-5472.CAN-09-1947.
[28] I.M. Helmy, A.M.A. Azim, Efficacy of ImageJ in the assessment of apoptosis, Diagn. Pathol. 7 (2012) 1–6, https://doi.org/10.1186/1746-1596-7-15.
[29] V.A. Sardão, P.J. Oliveira, J. Holy, C.R. Oliveira, K.B. Wallace, Tert-butylhydroperoxide–characterization of morphological features of cell death, BMC Cell Biol. 8 (2007) 1–15, https://doi.org/10.1186/1471-2121-8-11.
[30] S. Povea-Cabello, M. Oropesa-Ávila, P. de la Cruz-Ojeda, M. Villanueva-Paz, M. de la Mata, J.M. Suárez-Rivero, M. Álvarez-Córdoba, I. Villalón-García, D. Cotán, P. Ybot-González, J.A. Sánchez-Alcázar, Dynamic reorganization of the cytoskeleton during apoptosis: the two coffins hypothesis, Int. J. Mol. Sci. 18 (2017) 1–14, https://doi.org/10.3390/ijms18112393.
[31] Y.I. Yordanov, Hep G2 Cell culture confluence measurement in phase contrast micrographs – a user-friendly, open-source software-based approach, Toxicol. Mech. Methods 30 (2020) 146–152, https://doi.org/10.1080/15376516.2019.1695303.
[32] C.A. Schneider, W.S. Rasband, K.W. Eliceiri, Historical commentary nih image to imagej: 25 years of image analysis, Nat. Methods 9 (2012) 671–675, https://doi.org/10.1038/nmeth.2089.
[33] A. Valavanidis, T. Vlachogianni, C. Fiotakis, 8-hydroxy-2′ -deoxyguanosine (8-OHdG): a critical biomarker of oxidative stress and carcinogenesis, J. Environ. Sci. Health C Environ. Carcinog. Ecotoxicol. Rev. 27 (2009) 120–139, https://doi.org/10.1080/10590500902885684.
[34] J. Kopecka, S. Porto, S. Lusa, E. Gazzano, G. Salzano, A. Giordano, V. Desiderio, D. Ghigo, M. Caraglia, G. De Rosa, C. Riganti, Self-assembling nanoparticles encapsulating zoledronic acid revert multidrug resistance in cancer cells, Oncotarget 6 (2015) 31461–31478, https://doi.org/10.18632/oncotarget.5058.
[35] B.C. Evans, C.E. Nelson, S.S. Yu, K.R. Beavers, A.J. Kim, H. Li, H.M. Nelson, C. L. Duvall, Ex vivo red blood cell hemolysis assay for the evaluation of PH-responsive endosomolytic agents for cytosolic delivery of biomacromolecular drugs, J. Vis. Exp. (73) (2013) e50166, https://doi.org/10.3791/50166.
[36] C. Venter, C.U. Niesler, Rapid quantification of cellular proliferation and migration using ImageJ, Biotechniques 66 (2019) 99–102, https://doi.org/10.2144/btn-2018-0132.
[37] G. Carullo, A. Ahmed, A. Trezza, O. Spiga, A. Brizzi, S. Saponara, F. Fusi, F. Aiello, Design, synthesis and pharmacological evaluation of ester-based quercetin derivatives as selective vascular KCa1.1 channel stimulators, Bioorg. Chem. 105 (2020) 104404, https://doi.org/10.1016/j.bioorg.2020.104404.
[38] P. Mugnai, M. Durante, G. Sgaragli, S. Saponara, G. Paliuri, S. Bova, F. Fusi, L-Type Ca 2+ channel current characteristics are preserved in rat tail artery myocytes after one-day storage, Acta Physiol. 211 (2014) 334–345, https://doi.org/10.1111/apha.12282.
[39] S. Saponara, M. Durante, O. Spiga, P. Mugnai, G. Sgaragli, F. Fusi, Functional, electrophysiological and molecular docking analysis of the modulation of Cav1.2 channels in rat vascular myocytes by murrayafoline A, Br. J. Pharmacol. 173 (2016) 292–304, https://doi.org/10.1111/bph.13369.
[40] F. Fusi, F. Manetti, M. Durante, G. Sgaragli, S. Saponara, The vasodilator papaverine stimulates L-Type Ca2+ current in rat tail artery myocytes via a PKA-dependent mechanism, Vasc. Pharmacol. 76 (2016) 53–61, https://doi.org/10.1016/j.vph.2015.11.041.
[41] A. Ahmed, A. Trezza, M. Gentile, E. Paccagnini, A. Panti, P. Lupetti, O. Spiga, S. Bova, F. Fusi, Dynamin-independent CaV1.2 and KCa1.1 channels regulation and vascular tone modulation by the mitochondrial fission inhibitors dynasore and dyngo-4a, Eur. J. Pharmacol. 951 (2023) 175786, https://doi.org/10.1016/j.ejphar.2023.175786.
[42] F. Fusi, A. Ferrara, A. Zalatnai, J. Molnar, G. Sgaragli, Vascular activity of two silicon compounds, ALIS 409 and ALIS 421, novel multidrug-resistance reverting agents in cancer cells, Cancer Chemother. Pharm. 61 (2008) 443–451, https://doi.org/10.1007/s00280-007-0488-6.
[43] J. Jumper, R. Evans, A. Pritzel, T. Green, M. Figurnov, O. Ronneberger, K. Tunyasuvunakool, R. Bates, A. Žídek, A. Potapenko, A. Bridgland, C. Meyer, S.A. A. Kohl, A.J. Ballard, A. Cowie, B. Romera-Paredes, S. Nikolov, R. Jain, J. Adler, T. Back, S. Petersen, D. Reiman, E. Clancy, M. Zielinski, M. Steinegger, M. Pacholska, T. Berghammer, S. Bodenstein, D. Silver, O. Vinyals, A.W. Senior, K. Kavukcuoglu, P. Kohli, D. Hassabis, Highly accurate protein structure prediction with AlphaFold, Nature 596 (2021) 583–589, https://doi.org/10.1038/s41586-021-03819-2.
[44] B. Webb, A. Sali, Comparative protein structure modeling using MODELLER, Curr. Protoc. Bioinforma. 54 (2016) 5.6.1–5.6.37, https://doi.org/10.1002/cpbi.3.
[45] R.A. Laskowski, M.W. MacArthur, D.S. Moss, J.M. Thornton, PROCHECK: a program to check the stereochemical quality of protein structures, J. Appl. Cryst. 26 (1993) 283–291, https://doi.org/10.1006/jmbi.1996.0663.
[46] L.L.C. Schrödinger, The PyMOL Molecular Graphics System, v.1.8, 2015 (https://www.pymol.org/).
[47] J. Eberhardt, D. Santos-Martins, A.F. Tillack, S. Forli, AutoDock Vina 1.2.0: New docking methods, expanded force field, and python bindings, J. Chem. Inf. Model. 61 (2021) 3891–3898, https://doi.org/10.1021/acs.jcim.1c00203.
[48] G.M. Morris, R. Huey, W. Lindstrom, M.F. Sanner, R.K. Belew, D.S. Goodsell, A. J. Olson, AutoDock4 and AutoDockTools4: automated docking with selective receptor flexibility, J. Comput. Chem. 30 (2009) 2785–2791, https://doi.org/10.1002/jcc.21256.
[49] P.A. Kollman, I. Massova, C. Reyes, B. Kuhn, S. Huo, L. Chong, M. Lee, T. Lee, Y. Duan, W. Wang, O. Donini, P. Cieplak, J. Srinivasan, D.A. Case, T.E. 3rd Cheatham, Calculating structures and free energies of complex molecules: combining molecular mechanics and continuum models, Acc. Chem. Res. 33 (2000) 889–897, https://doi.org/10.1021/ar000033j.
[50] J. Gasteiger, M. Marsili, Iterative partial equalization of orbital electronegativity-a rapid access to atomic charges, Terahedron 36 (1980) 3219–3228.
[51] J. Franco Machado, M. Machuqueiro, F. Marques, M.P. Robalo, M.F.M. Piedade, M. H. Garcia, J.D.G. Correia, T.S. Morais, Novel "ruthenium cyclopentadienyl"-peptide conjugate complexes against human FGFR(+) breast cancer, Dalton Trans. 49 (2020) 5974–5987, https://doi.org/10.1039/d0dt00955e.
[52] I.C. Salaroglio, D.C. Belisario, M. Akman, S. La Vecchia, M. Godel, D.P. Anobile, G. Ortone, S. Digiovanni, S. Fontana, C. Costamagna, M. Rubinstein, J. Kopecka, C. Riganti, Mitochondrial ROS drive resistance to chemotherapy and immune-killing in hypoxic non-small cell lung cancer, J. Exp. Clin. Cancer Res. 41 (2022) 243, https://doi.org/10.1186/s13046-022-02447-6.

[53] J. Kopecka, M. Godel, S. Dei, R. Giampietro, D.C. Belisario, M. Akman, M. Contino, E. Teodori, C. Riganti, Insights into P-glycoprotein inhibitors: new inducers of immunogenic cell death, Cells 9 (2020) 1033, https://doi.org/10.3390/cells9041033.

[54] ASTM F756–00, Standard Practice for Assessment of Hemolytic Properties of Materials (ASTM International), West Conshohocken, PA, USA, 2004.

[55] A. Castellarin, S. Zorzet, A. Bergamo, G. Sava, Pharmacological activities of ruthenium complexes related to their NO scavenging properties, Int J. Mol. Sci. 17 (2016) 1254, https://doi.org/10.3390/ijms17081254.

[56] N. Mendes, F. Tortosa, A. Valente, F. Marques, A. Matos, T.S. Morais, A.I. Tomaz, F. Gärtner, M.H. Garcia, In vivo performance of a ruthenium-cyclopentadienyl compound in an orthotopic triple negative breast cancer model, Anticancer, Agents Med. Chem. 17 (2017) 126–136.

[57] V. Campani, I.C. Salaroglio, V. Nele, J. Kopecka, A. Bernkop-Schnürch, C. Riganti, G. De Rosa, Targeted self-emulsifying drug delivery systems to restore docetaxel sensitivity in resistant tumors, Pharmaceutics 14 (2022) 292, https://doi.org/10.3390/pharmaceutics14020292.

[58] A.L. Andrade, M.A. De Vasconcelos, V.D.S. Arruda, L.G. do Nascimento Neto, J.M. D.S. Carvalho, A.C.S. Gondim, L.G.F. Lopes, E.H.S. Sousa, E.H. Teixeira, Antimicrobial activity and antibiotic synergy of a biphosphinic ruthenium complex against clinically relevant bacteria, Biofouling 36 (2020) 442–454, https://doi.org/10.1080/08927014.2020.1771317.

[59] F.S. Gouveia Júnior, J.A.M. Silveira, T.M. Holanda, A.D. Marinho, L.A. Ridnour, D. A. Wink, R.J.B. de Siqueira, H.S.A. Monteiro, E.H.S. Sousa, L.G.F. Lopes, New nitrosyl ruthenium complexes with combined activities for multiple cardiovascular disorders, Dalton Trans. 52 (2023) 5176–5191, https://doi.org/10.1039/d3dt00059a.

[60] I. Maximiano, C. Henriques, R.G. Teixeira, F. Marques, A. Valente, A.M. M. Antunes, Lead to hit ruthenium-cyclopentadienyl anticancer compounds: cytotoxicity against breast cancer cells, metabolic stability and metabolite profiling, J. Inorg. Biochem. 251 (2024) 112436, https://doi.org/10.1016/j.jinorgbio.2023.112436.

Supplemental material

A novel combinatory treatment against a CDDP-resistant non-small cell lung cancer based on a Ruthenium(II) cyclopentadienyl compound

Iris C. Salaroglio[1], Denitsa Stefanova[2], Ricardo G. Teixeira[3], Nuno F.B. Oliveira[4], Amer Ahmed[5,§], Fabio Fusi[6], Virginia Tzankova[2], Yordan Yordanov[2], Miguel Machuqueiro[4], Simona Saponara[5], Andreia Valente[3,*], Chiara Riganti[1,*]

[1] Department of Oncology and Interdepartmental Molecular Biotechnology Center "Guido Tarone", University of Torino, Torino, Italy.

[2] Medical University of Sofia, Faculty of Pharmacy, Department of Pharmacology, Pharmacotherapy and Toxicology, 2 Dunav Str., 1000, Sofia, Bulgaria.

[3] Centro de Química Estrutural, Institute of Molecular Sciences and Departamento de Química e Bioquímica, Faculdade de Ciências, Universidade de Lisboa, Campo Grande, 1749-016 Lisboa, Portugal.

[4] BioISI – Instituto de Biossistemas e Ciências Integrativas, Departamento de Química e Bioquímica, Faculdade de Ciências, Universidade de Lisboa, Lisboa 1749-016, Portugal

[5] University of Siena, Department of Life Sciences, via Aldo Moro, 2, 53100, Siena, Italy.

[6] University of Siena, Department of Biotechnology, Chemistry and Pharmacy, via Aldo Moro 2, 53100, Siena, Italy.

§ Department of Bioscience, Biotechnology and Environment, University of Bari, Via Edoardo Orabona, 70125 Bari, Italy. (current address for A. Ahmed)

Corresponding authors

*E-mail: chiara.riganti@unito.it (C. Riganti)

amvalente@ciencias.ulisboa.pt (A.Valente)

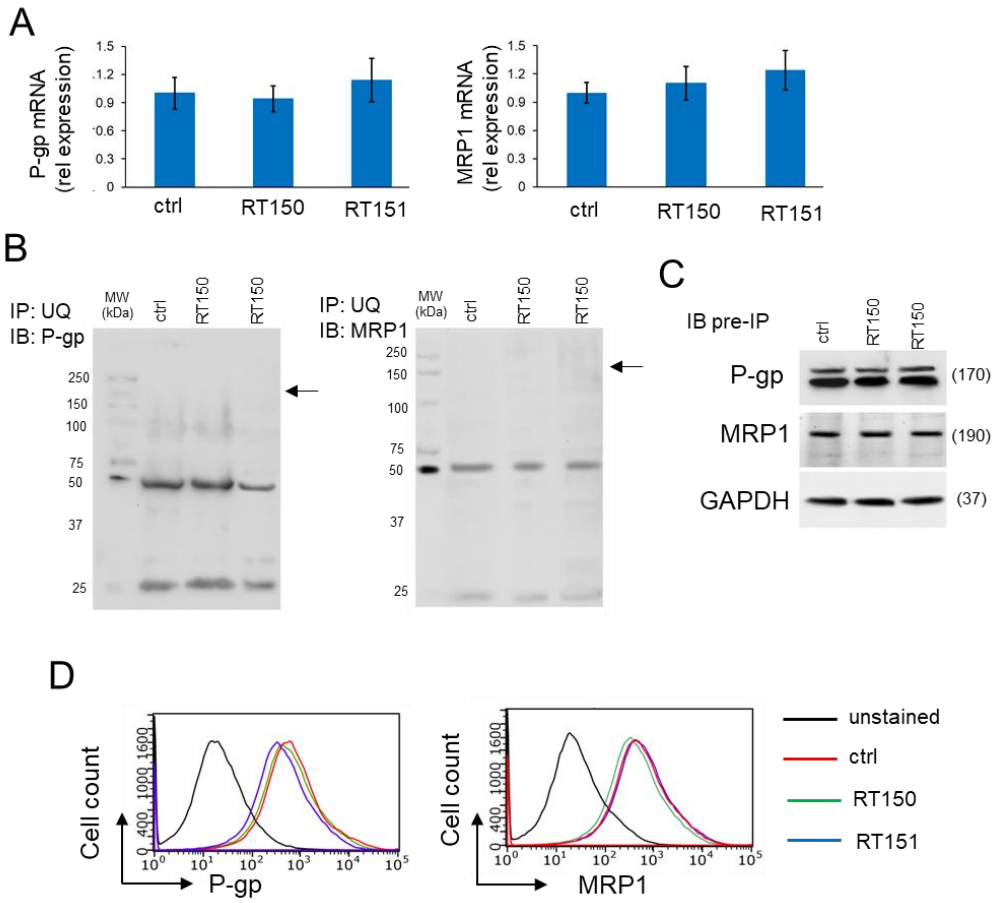

Supplementary Figure S1. Effects of RT150 and RT151 on P-gp and MRP1 expression in non-small cell lung cancer cells. NCI-H2228 cells were grown 24 h in fresh medium (ctrl) or in a medium 0.1 µM RT150 or RT151. **A.** P-gp and MRP1 mRNA levels measured by RT-PCR, in technical triplicates. Data are expressed as mean ± SD (n=3 independent experiments). **B.** Whole cell lysates were immunoprecipitated (IP) with an anti-ubiquitin antibody, then immunoblotted (IB) for Pgp and MRP2. Arrows: expected P-gp and MRP1 bands. The blot is representative of 1 out of 3 independent experiments. **C.** An aliquot of whole cell lysates before immunoprecipitation was directly immunoblotted (IB pre-IP) for P-gp and MRP1, as indexes of equal amounts of proteins used for immunoprecipitation and amount of P-gp and MRP1 present in whole cell lysates. GAPDH was used as control of equal protein loading. The blot is representative of 1 out of 3 independent experiments. **D.** Levels of P-gp and MRP1 present on cell surface, measured by flow cytometry in technical duplicate. Unstained: cells not incubated with the anti-P-gp or anti-MRP1 antibody, as index of cellular autofluorescence. The histograms are representative of 1 out of 3 independent experiments.

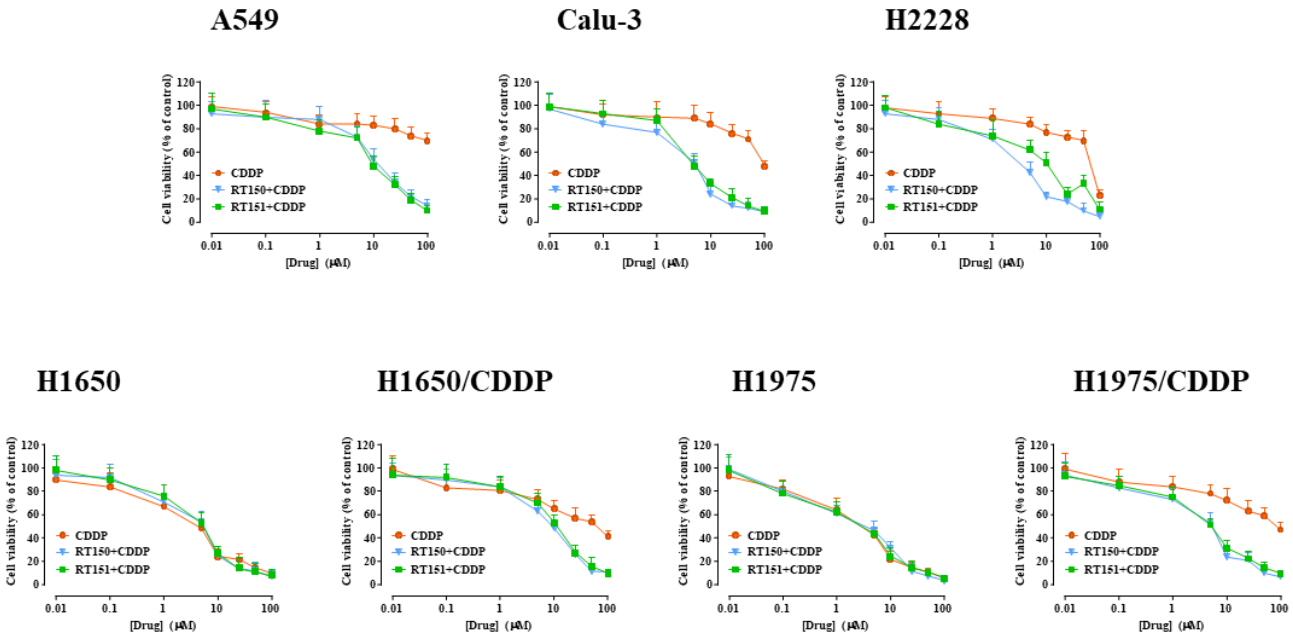

Supplementary Figure S2. Dose-response effect of RT150 and RT151 on viability of non-small cell lung cancer cells. Viability was measured by MTT assays in rA549, Calu-3, NCI-H2228, NCI-H1650, NCI-H1650/CDDDP, NCI-H1975 and NCI-H1975/CDDP cells, treated for 72 h with compound cisplatin (CDDP) alone or combined with **RT150** or **RT151** in the range of concentrations of 0.01 µM, 0.1 µM, 1 µM, 5 µM, 10 µM, 25 µM, 50 µM, and 100 µM. Data are mean±SD (n=3 independent experiments).

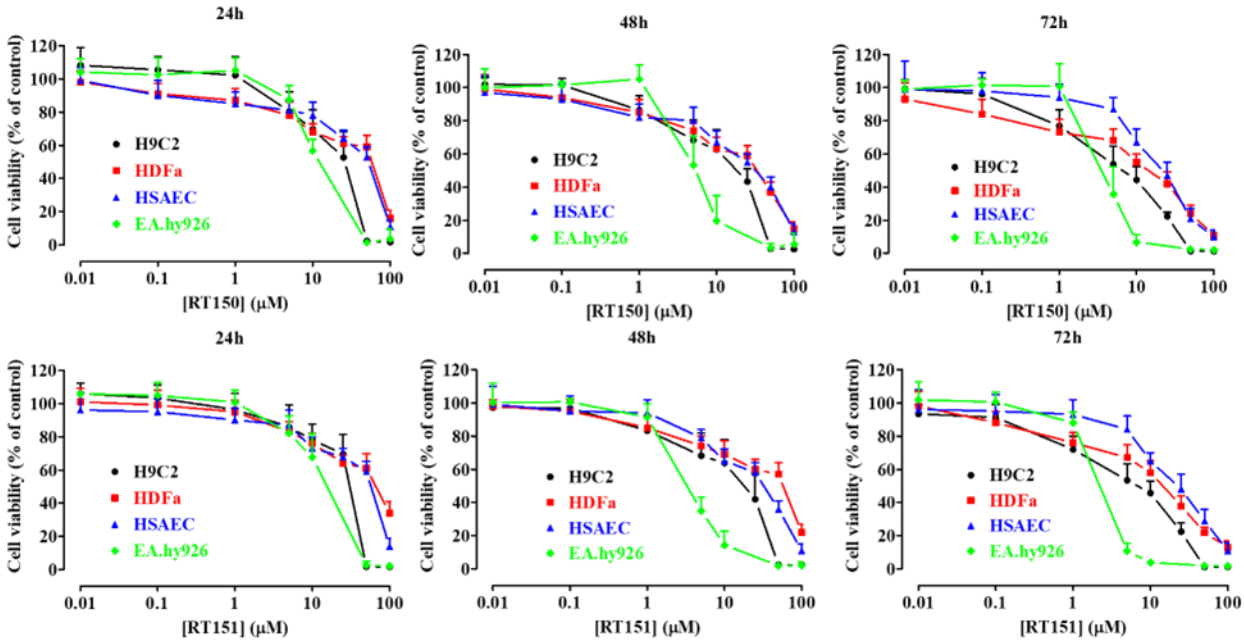

Supplementary Figure S3. Dose-response effect of RT150 and RT151 on viability of non-transformed cells. Viability was measured by MTT assays in rat cardiomyoblasts (H9c2), human dermal adult fibroblasts (HDFa), human small airway epithelial cells (HSAEC) and endothelial (EA.hy926) cells, treated for 24 h, 48 h or 72 h with compound **RT150** and **RT151** in the range of concentrations of 0.01 µM, 0.1 µM, 1 µM, 5 µM, 10 µM, 25 µM, 50 µM, and 100 µM. Data are mean±SD (n=3 independent experiments).

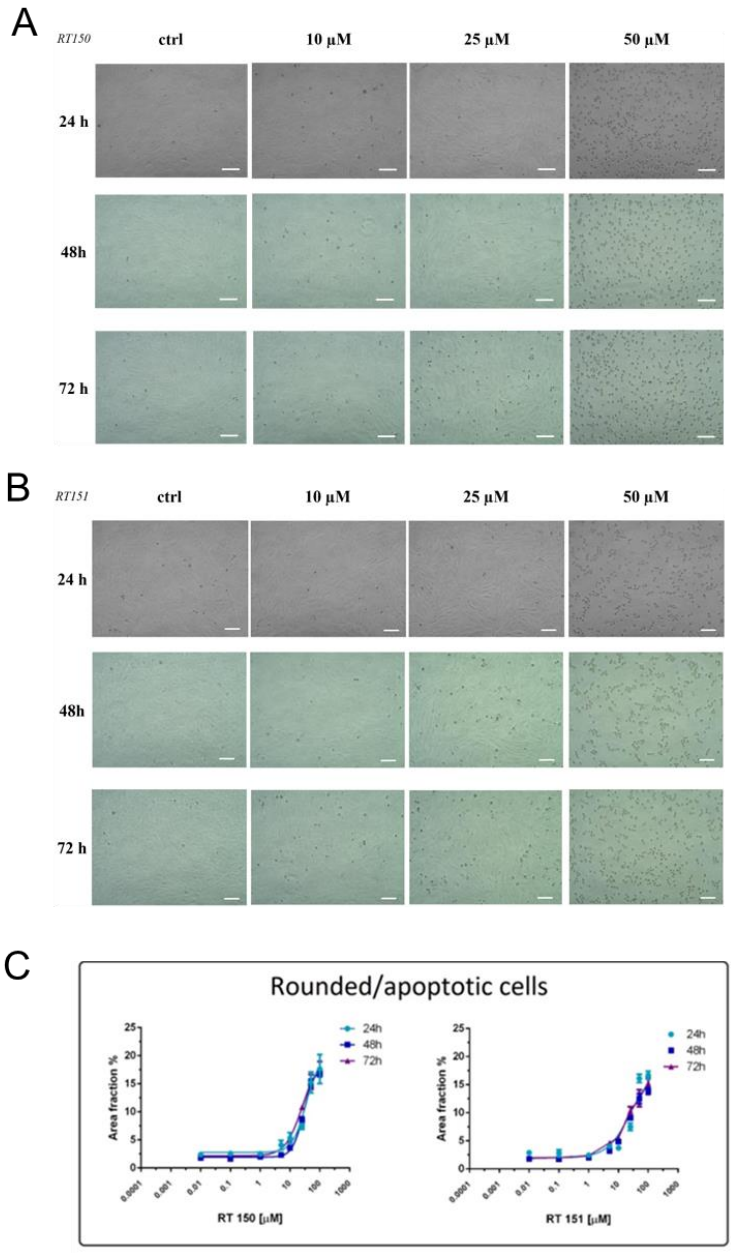

Supplementary Figure S4. Apoptosis in cardiomyoblast H9c2 cells.

Representative phase contrast micrographs of H9c2 cells, treated for 24 h, 48 h or 72 h with compound **RT150** (**A**) and **RT150** (**B**) at 10 µM, 25 µM, and 50 µM. Ocular: 10x; Objective: 10x. Bar: 100 µm. **C.** Quantification of the rounded cell measurement assays. Concentrations of **RT150** and **RT151** are 0.01 µM, 0.1 µM, 1 µM, 5 µM, 10 µM, 25 µM, 50 µM, and 100 µM. Data are mean±SD (n=3 independent experiments).

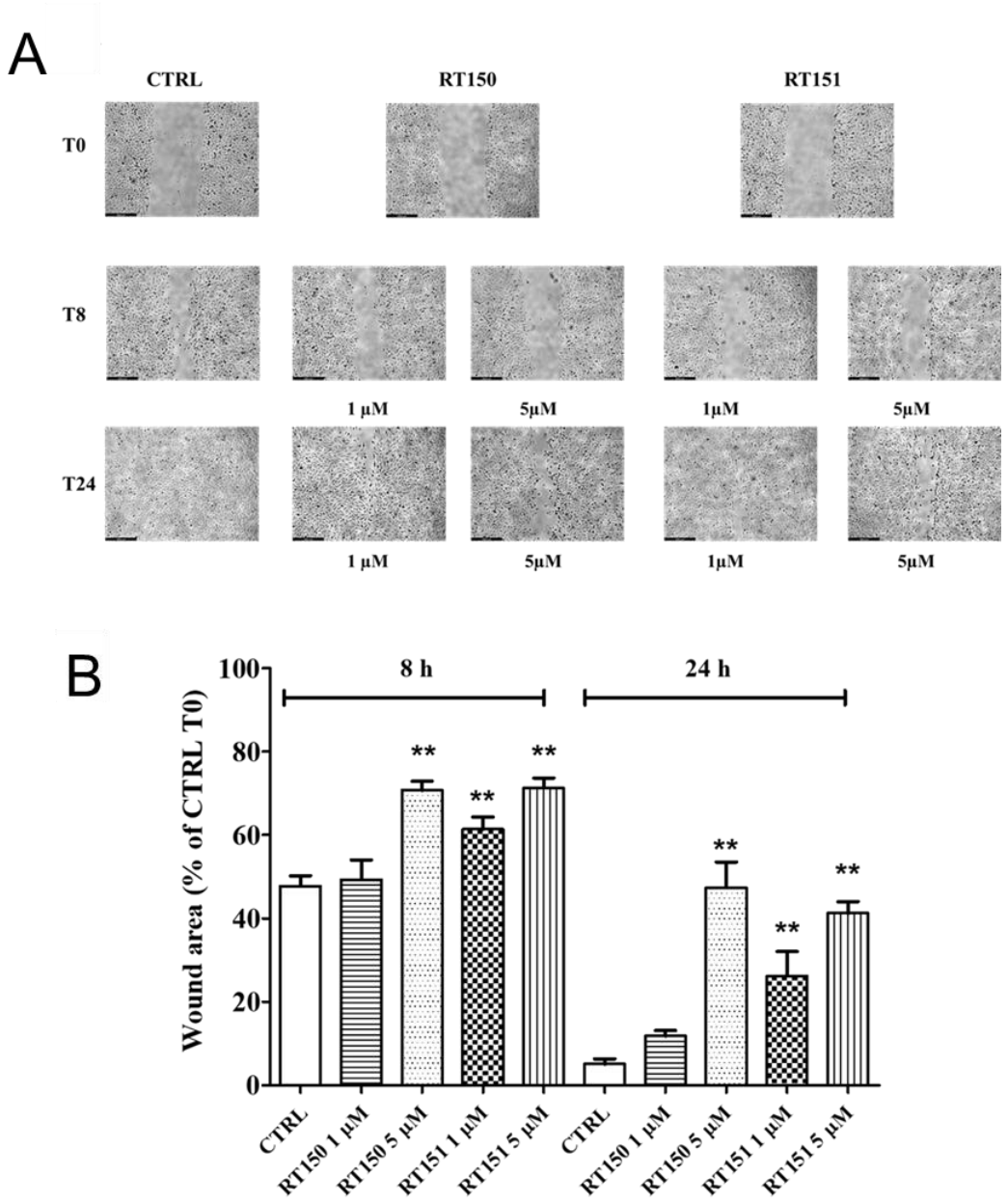

Supplementary Figure S5. RT150 and RT151 reduce migration of EA.hy926 cells. A. Representative pictures of scratch closure in EA.hy926 cell. Scale bar 358.4 µm. **B.** Quantification of wound healing scratch assay. The results are reported as the percentage of opened area over basal control (CTRL) after 8 and 24 h, in triplicates. Data are mean±SD (n=3 independent experiments). **p < 0.01: vs. CTRL

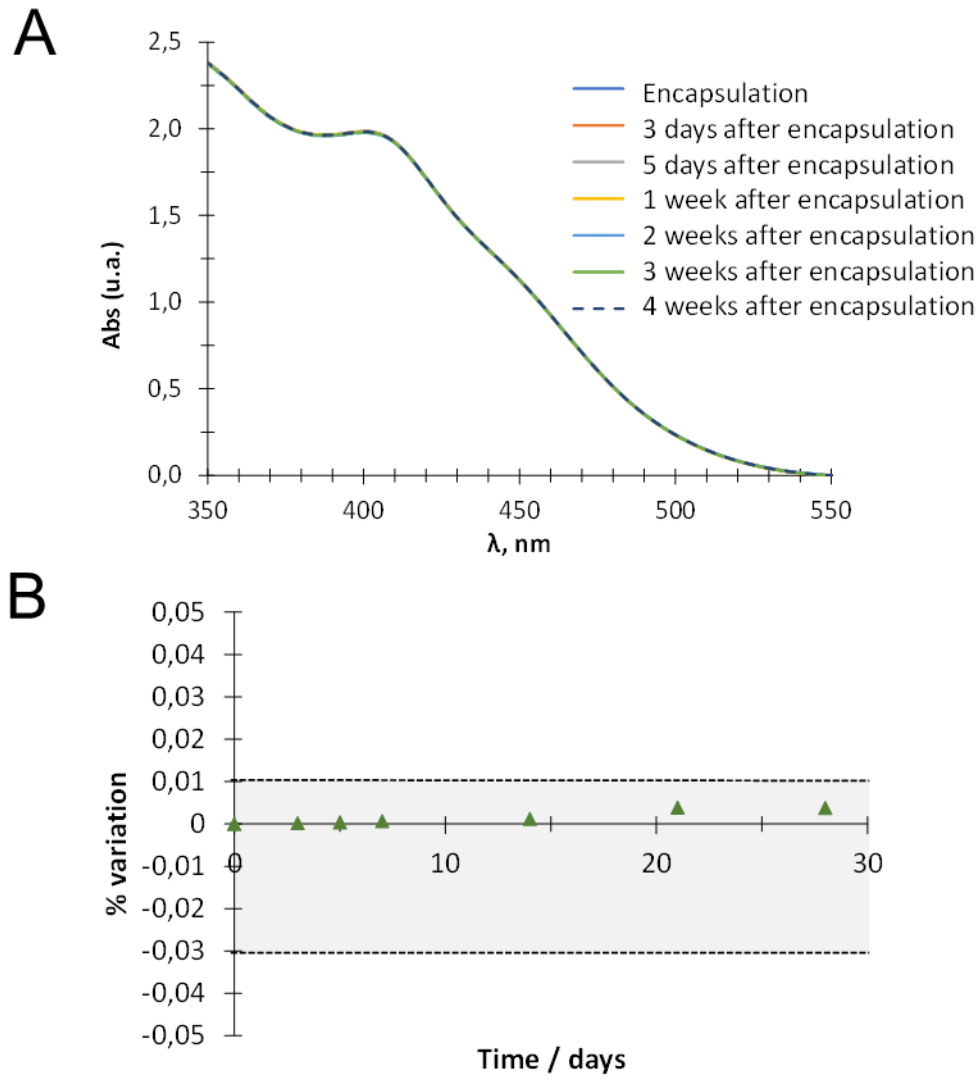

Figure S6. Stability studies in water for RT151. A. UV-Vis spectra during the period of assay **B.** Percentage of variation along time (λ = 405 nm; 1 cm optical path).

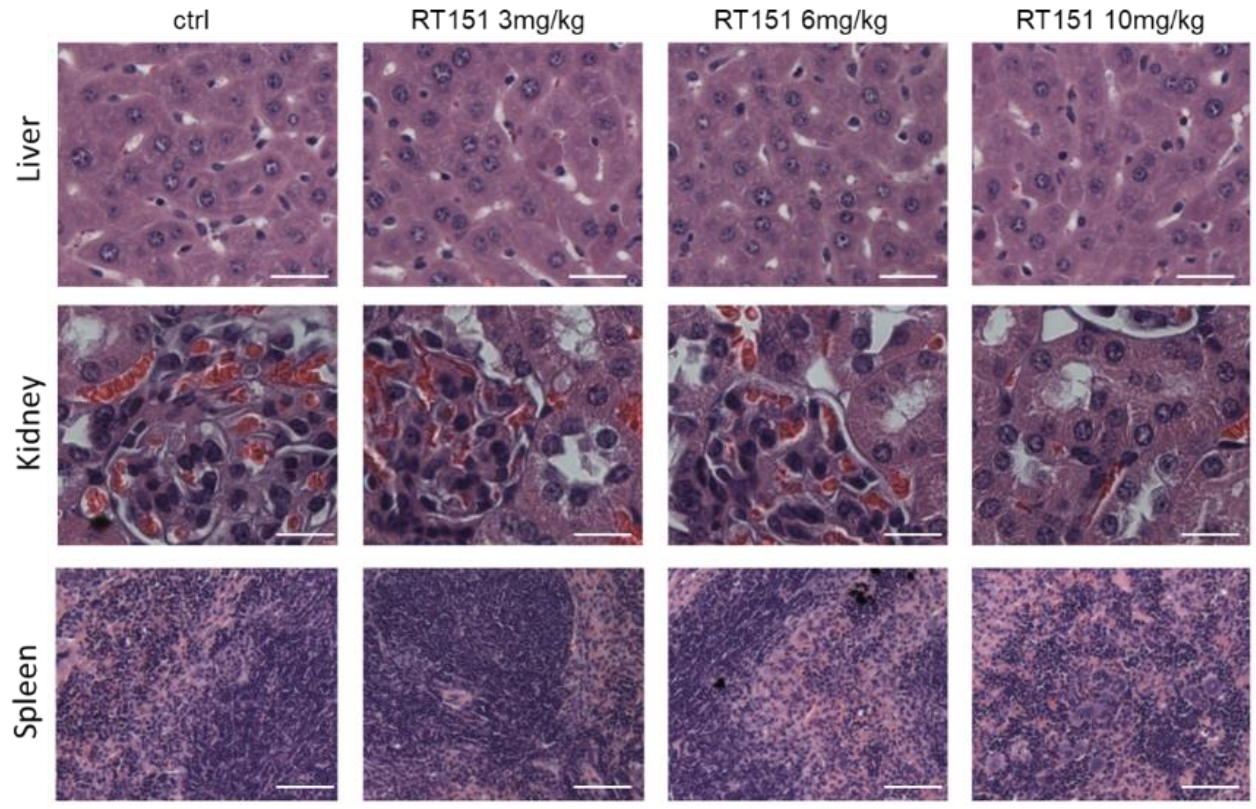

Figure S7. *Post-mortem* pathology analysis of liver, kidney and spleen in mice treated with increasing doses of RT151. NSG mice were treated 6 weeks (once/week) with Captisol® intravenously (i.v.), 3, 6 or 10 mg/kg **RT151** i.v., then sacrificed at day 49. Representative hematoxylin-eosin stains of liver, kidneys and spleen sections. Ocular: 10X; Objective: 20X (liver, lung, kidney); 10X (spleen). Bar: 50 µm.